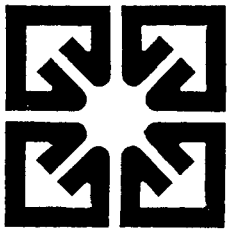

SUPERCOMPUTER COMPUTATIONS RESEARCH INSTITUTE

ELectromagnetic and MUon Detector for the SSC

by

M. Fortner, D. Hedin, S. Linn,
E.M. Wang, D. Winn, and H. Yamamoto

FSU-SCRI-91T-15

February 19, 1991

THE FLORIDA STATE UNIVERSITY
TALLAHASSEE, FLORIDA

DISCLAIMER

FSU-SCRI-91-15
LBL-30297

An ELectromagnetic and MUon Detector for the SSC†

M. Fortner and D. Hedin
Physics Dept., Northern Illinois University
Dekalb, IL 60115

S. Linn
SCRI, Florida State University
Tallahassee, FL 32306

E. M. Wang
Lawrence Berkeley Laboratory
Berkeley, CA 94720

D. Winn
Physics Dept., Fairfield University
Fairfield, CT 06430

H. Yamamoto
Physics Dept., University of California Los Angeles
Los Angeles, CA 90024

ABSTRACT

This report presents a study of the design and capabilities of a detector specialized in measuring high-P_t leptons and photons from high energy pp collisions. The detector consists of a precision electromagnetic calorimeter, a tracker and pre-radiator device, and a robust muon spectrometer. The primary physics goal of this device is searching for Higgs boson through the decays $H \rightarrow \gamma\gamma$, $H \rightarrow ZZ^*$, and $H \rightarrow ZZ$.

† This research was sponsored by US Department of Energy Contracts DE-AC02-89ER40514, DE-AC02-87ER40368, DE-FC05-85ER250000, DE-AC03-76SF00098 and DE-AT03-88ER40384

I. INTRODUCTION

The short history of experimental particle physics is often summarized by a list of important experiments whose data contributed enormously to our current understanding of nature. With few exceptions, these experiments used leptons as probes or final state signatures. Because the primary interaction for the light charged leptons(e, μ) is electromagnetic, theoretical production is more easily understood and experimental detection is easier. Moreover, a detector capable of identifying these leptons will also be highly sensitive to detection of the electro-weak gauge bosons(γ, Z, and W) which, besides being carriers of force, hold some promise for being carriers of new physics. For these reasons, lepton and photon detection at the SSC is expected to continue to provide the most convincing evidence for new phenomena.

General purpose detectors are designed for broad-band sensitivity to anticipated physics. Typically this means a large complex detector with many systems whose optimization requirements conflict. For example, detectors that emphasize hermetic measurement of hadronic energy usually compromise electromagnetic calorimetry, because the necessary support structures create dead areas. Also, it is not well understood how to optimize resolution in both electromagnetic and hadronic calorimetry. Further, large detectors present a formidable triggering problem. Because the event size is large, it follows that fewer events can be permanently logged for careful offline scrutiny. With the high interaction rates and small cross sections expected at the SSC, this means that trigger thresholds will be set at higher than optimum values and some physics will be lost, especially at lower mass scales. If both magnetic tracking inside the calorimeter and hadronic calorimetry are not used, it is possible to design a relatively simple experiment of moderate cost that is optimized for electron, photon, and muon detection which is capable of sustained data accumulation in a high luminosity environment. Such a detector would complement large detectors and allow precise measurement of many physics signals and confirmation of others.

This report presents a detector specialized for electrons, photons, and muons. Part of this study was done at Snowmass '90 in the sub-group which examined high luminosity and specialized detectors. The report is separated into four sections. In Section I, the overall detector philosophy is presented along with the salient hardware features and the physics goals. Section II describes detailed Monte Carlo studies of the expected SSC physics processes which were used to determine the detector parameters. Section III contains a more thorough discussion of the detector characteristics, capabilities, limitations, and cost. Some topics are detailed in a set of appendicies.

The direct observation of phenomena associated with the source of electro-weak symmetry breaking has been stated as a major scientific goal of the SSC program. Operationally, this translates to standard model neutral Higgs boson searches for Higgs masses of about 100 GeV to 1 TeV. This subject will be the focus of the report. This challenging experimental task will be used to establish a number of detector performance goals. In particular, capabilities of a detector designed for the observation of a standard model neutral Higgs boson in the intermediate and heavy mass regions will be described in detail. The ability to reliably detect the Higgs over the full mass range will be shown to be more than adequate for many other physics topics.

The use of specialized detectors for Higgs searches has been discussed many times over the last decade. Usually, the studies have focused on muons[I.1] with the

emphasis on detecting $H \rightarrow ZZ \rightarrow 4\mu$ at the highest luminosities. Without electron detection, the loss in available branching ratio in the four lepton channel outweighs any advantages of a muon-only detector and precludes systematic comparison of electron to muon channels. It has also been pointed out by many authors[I.2] that, depending on the number of Higgs and their masses, the $H \rightarrow \gamma\gamma$ channel may be the only detectable mode. Searching for Higgs' decay in this channel requires not only excellent energy resolution and particle identification, but also the ability to record a large sample of events. To satisfy all of these may require a specialized detector.

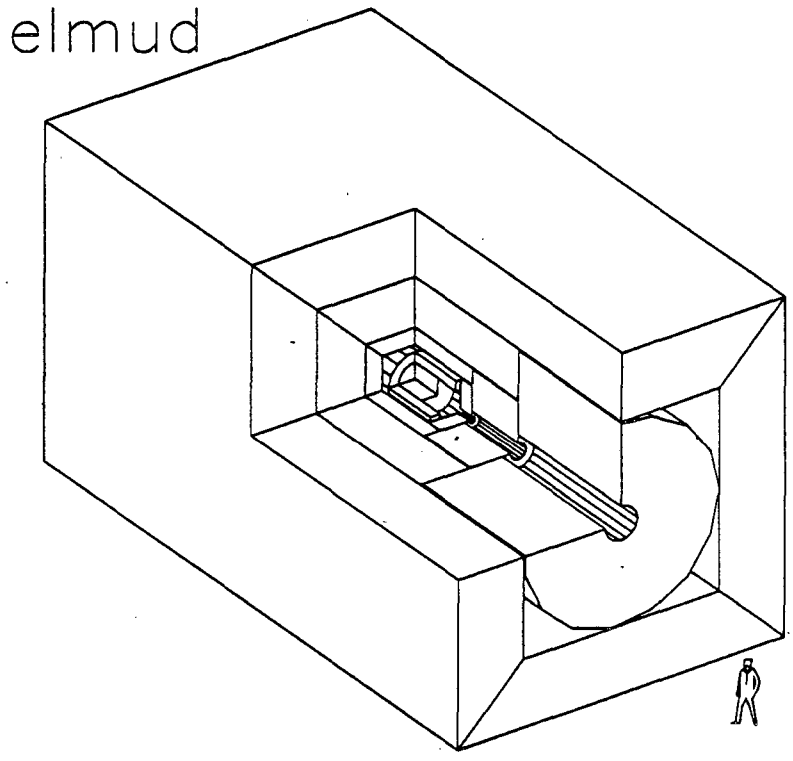

Fig. I.1 Sectional view of ELMUD

A detector optimized for electromagnetic(EM) shower and muon detection, ELMUD [I.0] for short will now be described. The detector in a cutaway view is shown in Figure I.1. The parameters of the detector are driven by considerations of angular coverage, resolution, particle identification, and triggering. The EM shower detector consists of a pre-radiator tracking detector and a precision EM calorimeter which covers only the central rapidity region($|\eta| < 1.5$). Outside is a thick iron muon spectrometer with large solid angle coverage ($|\eta| < 3$) and good resolution. Ideally, Higgs searches in lepton modes would require $|\eta| < 3$. If the EM coverage is limited to $|\eta| < 1.5$, then problems with high precision performance in a high radiation environment and increased electron/photon identification difficulties are avoided. The proposed layout of central electromagnetic and complete muon coverage is a

compromise between these considerations. It still more than doubles the acceptance for the $H \rightarrow ZZ \rightarrow 4l$ channel while providing precision energy resolution and good acceptance for states such as $H \rightarrow \gamma\gamma$ or $Z' \rightarrow ee$.

The Higgs channels set the energy resolution goals. For the electromagnetic detector, considerations of $H \rightarrow \gamma\gamma$ require energy resolutions of 1% or better for photon energies of the order of 80-150 GeV. A number of different technologies can meet this goal but with different tradeoffs. For example, barium fluoride has superior resolution but has a larger Moliere radius than lead-scintillating fiber. Using barium fluoride will then either cause a degradation in particle identification or force the detector to begin at a larger radius. For this initial exercise, an electromagnetic calorimeter made using lead and plastic scintillating fibers was assumed. It consists of towers of 0.1 in η and 0.05 in ϕ read out in single, 27 radiation length thick (1 λ) towers. An energy resolution of $\Delta E/E = 0.005 \oplus 0.07/\sqrt{E}$ was assumed ($\oplus$ indicates addition in quadrature). A more exotic and interesting EM calorimeter made of lead fluoride, also appears to meet these requirements. The muon resolution needs are less stringent. Considerations of the backgrounds of both lower mass $H \rightarrow ZZ^*$ and high mass $H \rightarrow ZZ$ require momentum resolutions of from (7-10)%. This can be met with 3-6 m thick iron toroids.

A critical requirement for ELMUD is to have sufficient particle identification for the signal channels of interest. The thick iron toroids will provide sufficient muon identification. Backgrounds to high P_t electrons are reduced by isolation cuts in the calorimeter and matching between the tracker and the calorimeter. In order to reduce the background events from jets, a pre-radiator device is needed to identify false photon candidates due to multiple π^0s that cannot be resolved by the calorimeter alone.

All components are chosen to withstand the highest luminosity that the SSC will be capable of achieving. Because the tracking and calorimeters start at small radii and are relatively small, the muon detector defines boundaries comparable to a present day collider detector. It follows that the cost will not be considerably different.

In addition to reduced cost, a small simple detector has advantages in triggering. Both the calorimeter and muon triggers will utilize local quantities such as an isolated calorimeter cluster above an E_t threshold. This will allow level-1 trigger decisions to be done locally and in parallel. ELMUD's channel count will give an event size less than 50 kbytes. This is about 50 times smaller than that estimated for large general purpose detectors. This both reduces the burden on the later stages of the trigger and allows more events to be permanently stored. Some moderate estimates of bandwidth lead us to the conclusion that the detector could be read out at a rate exceeding several hundred Hz.

With ELMUD, the case for a detector that is relatively simple, inexpensive and robust is being made. The Standard Model has been the guide, simplicity has been the approach. Higgs physics sensitivity demands high precision lepton energy measurement, high rate event readout, and high luminosity resilience. These requirements are simultaneously met with a simple and conservative design. ELMUD requires minimal technological extrapolation. ELMUD also requires minimal lead time and can use the latest technology available. In short, the opportunity for a minimal risk experiment which gets "to the heart of the matter" is the essence of ELMUD.

Detector Overview

1. Tracker and Pre-radiator
   - Three superlayers of $750\mu m$ plastic scintillating fibers
   - Two axial and two stereo layers/superlayer
   - Two layers scintillating pads
   - 7 mm tungsten radiator
   - $40\ cm \leq r \leq 50\ cm$, $|z| \leq 100\ cm$
   - $|\eta| \leq 1.5$
   - z-vertex resolution ≤ 0.5 cm
   - $r - \phi$ resolution/superlayer= 0.01 cm
   - z-coordinate resolution/superlayer= 0.1 cm
   - Channel count = 98k (packed data 13 kb)
   - Cost \$9M
2. Calorimeter
   - PSF/Pb construction
   - Segmentation $0.05 \times 0.10(\phi \times \eta)$ projective
   - Thickness 27 X_0 , 1 λ
   - $50\ cm \leq r \leq 100\ cm$, $|z| \leq 100\ cm$
   - $|\eta| \leq 1.5$
   - Resolution $0.005 \oplus 0.07/\sqrt{E}$
   - Channel count = 4k (packed data 16 kb)
   - Cost \$7M
3. Muon spectrometer
   - Iron toroids and proportional drift tubes
   - $r \leq 700\ cm$, $|z| \leq 1550\ cm$
   - $|\eta| \leq 3.0$
   - Resolution 10%(m.c.s.), $0.2P_t$(TeV)
   - Channel count = 38k (packed data 6 kb)
   - Cost \$33M
4. Trigger and Data Acquisition
   - level-1, analog devices, rate = $2 \times 10^4\ Hz$
   - level-2, digital signal processors, rate = $2 \times 10^2\ Hz$
   - level-3, processor farm, rate = $2 \times 10^0\ Hz$
   - Cost \$8M

II. PHYSICS

II.A Standard Model Higgs Searches

The design goals of ELMUD have been restricted to what is necessary for finding Standard Model Higgs bosons over the mass range 0.1-1.0 TeV in the most direct manner. This requires sensitivity to at least the following decay modes:

1. $H \rightarrow \gamma\gamma$.
2. $H \rightarrow Z + Z^*$.
3. $H \rightarrow Z + Z$.

The properties of the postulated Higgs bosons define a wide range of experimental requirements. Table II.1 below summarizes these properties.

Table II.1 Higgs Properties

Mass [GeV]	150	200	400	800
Width [GeV]	< 1	2	30	250
Rate [Events/10^4 pb^{-1}]	250 (1500)	600	500	50

Rates are for $M_{top} = 140$ GeV and 4 lepton decay mode.
() 2γ decay mode.

The Higgs boson can range from a very *narrow* low mass resonance up to a very *broad* high mass (non)resonance. In addition, the event rates expected at high mass are vanishingly small at SSC design luminosity. The table suggests that both high energy resolution and high position resolution are needed for the low mass searches. More modest resolution and possibly high luminosity resilience are needed for high mass searches because of limited statistics. If the mass is high enough where no resonance appears more detailed studies, such as the polarization of the Z-bosons, might be needed in order to establish whether events are consistent with Higgs decays. In all cases, a Higgs detector needs to be as efficient as possible.

The parameters of the detector were established so that adequate Higgs sensitivity was achieved for the full mass range. To examine the detection ability of ELMUD for a wider class of physics processes; extra gauge bosons, top, and lepton compositeness were also studied. These topics are discussed in appendices; where the performance is shown to be quite adequate.

II.B $H \rightarrow \gamma\gamma$

This decay mode has been studied before[II.1-5]; however, the issues of energy and vertex position resolution have been revisited. In addition, QCD backgrounds and triggering issues have been thoroughly studied for the first time. The backgrounds consist of continuum two-photons, photon-jet, and two-jet events where the jets can fluctuate into localized EM energy depositions that are interpreted as a photon. The analysis of both signal and background is done by finding the two highest E_t isolated clusters in an EM calorimeter and reconstructing the invariant mass. The Higgs' mass range covered is 80-160 GeV. For resolution studies, only the intrinsic two-photon background was used. The QCD background is treated separately.

The two-photon invariant mass spectra for signal plus continuum (the most ideal case), where the photon energies have been smeared to simulate the effects of energy resolution, appear in Figures II.1a-f for a 90 GeV Higgs and Figures II.2a-f for a 150 GeV Higgs. Clearly, for 90 GeV, the continuum background is quite substantial. The two-photon mass spectra for perfect energy resolution but with the z-vertex position smeared appear in Figures II.3a-c, for σ[vertex] = 1, 2, and 7 cm, for a 150 GeV Higgs. The latter case is equivalent to no z-vertex position determination and is clearly not acceptable. Together, a vertex determination of < 1 cm and an energy resolution of $0.005 \oplus 0.07/\sqrt{E}$ give comparable Higgs widths (about 1 GeV) and represent a upper bound to what is an acceptable mass resolution.

In addition to the continuum two-photon background, the photon-jet and two-jet QCD backgrounds have been studied. The fake two-photon background arises from jets fragmenting into isolated electromagnetic clusters interpreted as a photon(See Figure II.4). The fluctuation of a jet to a *single* π^0, aside from fragmentation and statistical uncertainties, is found to be about 10^{-4} of the cross section. The fluctuation of a jet into multiple π^0s, where the π^0s are collimated, can be several times larger. When this probability is applied to two jets, the background is found to be a order of magnitude larger than predicted by considering only jet to single π^0s. Failure to reject a large fraction of these events may result in much more QCD background than estimates from jet to single π^0 probabilities. A simple EM calorimeter simulation was done to estimate the size of these effects and to determine if experimental techniques could be developed to reduce these backgrounds: Energy isolation is the scalar sum of the transverse energy in a cone R=0.5 around the center of the EM cluster after the cluster E_t has been subtracted. The cluster must be isolated from all tracks, charged and neutral, except in the region where conversions and albedo produce hits from single photons ($d\theta < 20mr$). Finally, the cluster shape must be consistent with a single electron or photon. The table below summarizes the effects of these cuts on the above backgrounds where the jet can fluctuate into one or more π^0s.

Since the signal is comparable to the intrinsic two-photon continuum, the jet backgrounds need to be rejected to at least this level. It is essential to measure isolation, shower shape, and to veto EM clusters that have more than one charged or neutral tracks in their vicinity. The set of cuts defined above accomplish this; however, a fine-grained calorimeter and pre-radiator are necessary but perhaps even *insufficient* for the lower mass ($M_H = 90\ GeV$) cases. It is noteworthy that for M_H near M_Z, it is necessary to reject $Z \rightarrow ee$ to better than 10^{-3} or Z-bosons themselves become backgrounds.

Table II.2 2γ Background Rejection

Process Cross section	$\gamma+\gamma$ [pb]	γ+j [pb]	j + j [pb]
1. Raw [Pythia 4.9]:			
$m_{2\gamma,\gamma+j,j+j} \geq$ 50,80,100 GeV	68	$23 \cdot 10^3$	$76 \cdot 10^6$
2. Kinematics: $P_{t,\text{cell}} > 40GeV^*$,			
$\lvert\eta\rvert < 1.5^{**}$,			
$130 < M_{2\text{cell}} < 170$ GeV	1.2	130	$46 \cdot 10^3$
3. Calorimeter Isolation:			
$\Sigma E_t < 5$GeV, R=0.6	1.2	7.3	140
4. Tracking Isolation:			
$d\theta > 20$ mr	1.2	0.74	1.51
5. Shower Shape:			
	1.2	0.56	0.85

* Binned cells in 0.05x0.05 = $\Delta\eta$ x $\Delta\phi$

** The Higgs is produced nearly at rest so a rapidity cut is equivalent to a cut in $cos\theta^*$ used by others.

Table II.3 2γ Analysis Summary

Process	σ [pb] raw	Phy. Cuts	σ [pb] after	Detector Cuts	σ [pb] final
$H \rightarrow \gamma\gamma$		$\lvert\eta\rvert < 1.5$ $P_{t,\gamma} > 40\ GeV$ $\Sigma E_t < 5\ GeV, R = 0.6$ $140 < M < 160\ GeV$		$d\theta[2\pi^0] > 20$mr shower shape track veto 1% mass bin	
M=150 GeV	$1.4 \cdot 10^{-1}$		$5.4 \cdot 10^{-2}$		$5.4 \cdot 10^{-2}$
$qq + gg \rightarrow \gamma\gamma$	$7.0 \cdot 10^1$	"	$1.2 \cdot 10^0$	"	$7.3 \cdot 10^{-2}$
γ+ jet	$2.3 \cdot 10^4$ [a]	"	$3.7 \cdot 10^0$	"	$2.2 \cdot 10^{-2}$
jet + jet	$7.6 \cdot 10^7$ [b]	"	$7.0 \cdot 10^1$	"	$3.1 \cdot 10^{-2}$
$qg \rightarrow q\gamma\gamma$	$8.5 \cdot 10^1$ [c]	"	$5.2 \cdot 10^{-2}$ [d]	"	$4.0 \cdot 10^{-3}$

Generator level cut: [a] $\sqrt{\hat{s}} > 80\ GeV$, [b] $\sqrt{\hat{s}} > 100\ GeV$

[c] Used: $\sigma = 2.5 \cdot \sigma_{\gamma\gamma}$

[d] Kinematic cut factor for γ+ jet=0.0061 and isolation cut factor=0.1

It is necessary to have a high trigger rate capability so that an efficient and unbiased $H \rightarrow 2\gamma$ search is possible. To achieve this it will be necessary to have a higher level trigger which uses global information from the event. The requirement of two isolated EM clusters with 20 GeV P_t threshold gives a rate of about 100 Hz for QCD two-jet events at a luminosity of $10^{33} cm^{-2} sec^{-1}$. Clearly such a requirement is satisfactory for readout of Z-bosons as well. Triggering will be discussed in more detail in section III.E.

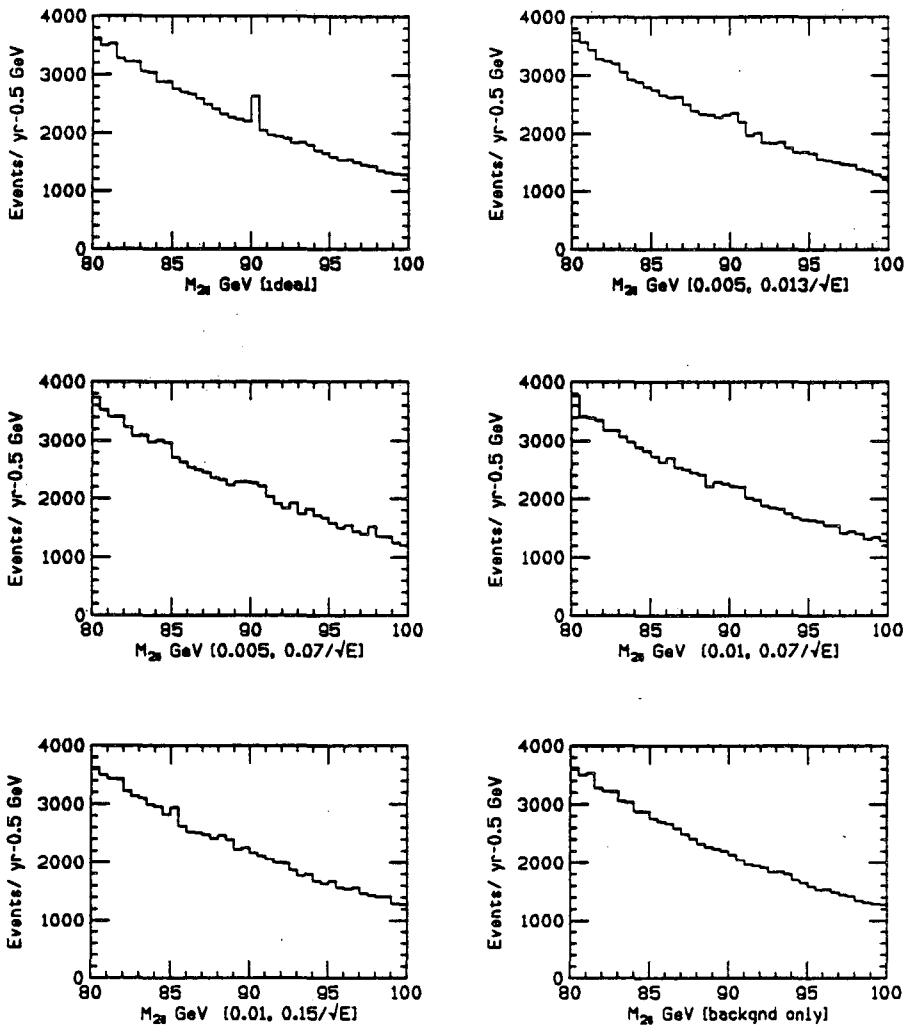

FIG. II.1 $M_{2\gamma}$ for 90 GeV Higgs as seen with different calorimeter resolutions.(a) Ideal, (b) $0.005 \oplus 0.07/\sqrt{E}$, *(c)*$0.01 \oplus 0.07/\sqrt{E}$, *(d)*$0.005 \oplus 0.013/\sqrt{E}$ *(e)*$0.01 \oplus 0.15/\sqrt{E}$, *(f) no signal. Background shown is continuum $\gamma\gamma$ only. The events must pass $P_{t,\gamma} > 20$ GeV threshold in* ELMUD *geometry.*

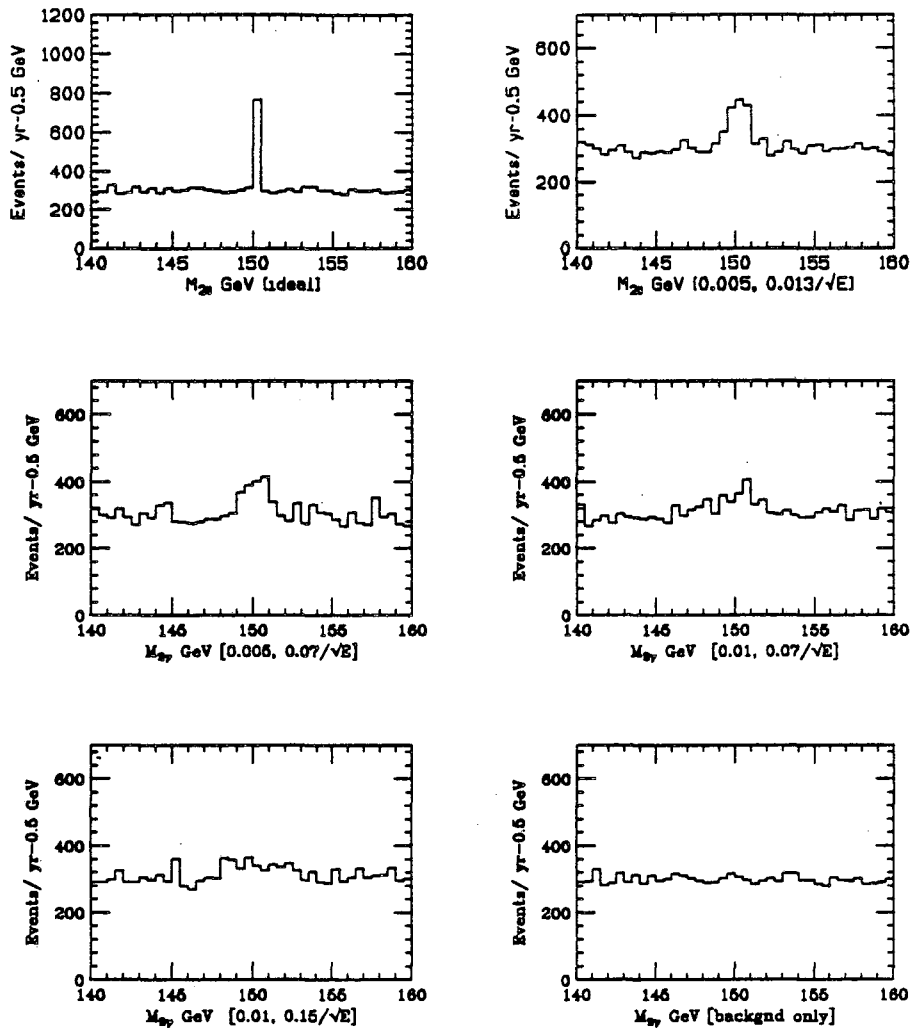

FIG. II.2 $M_{2\gamma}$ for 150 GeV Higgs as seen with different calorimeter resolutions described in Fig II.A.1. Background shown is continuum $\gamma\gamma$ only. The events must pass $P_{t,\gamma} > 20$ GeV threshold in ELMUD *geometry.*

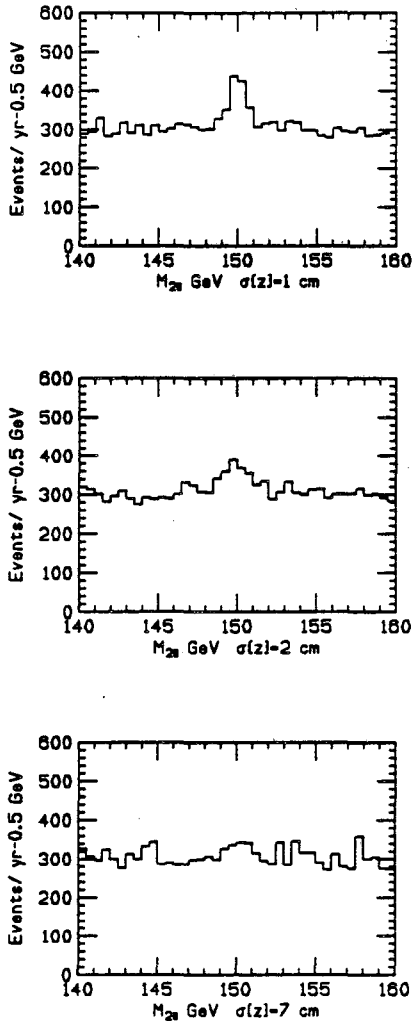

FIG. II.3 $M_{2\gamma}$ for 150 GeV Higgs as seen with different z vertex resolutions (a)σ_z = 1 cm, (b)σ_z = 2 cm and (c)σ_z = 7 cm. Case (c) is equivalent to no event vertexing. Background shown is continuum $\gamma\gamma$ only.

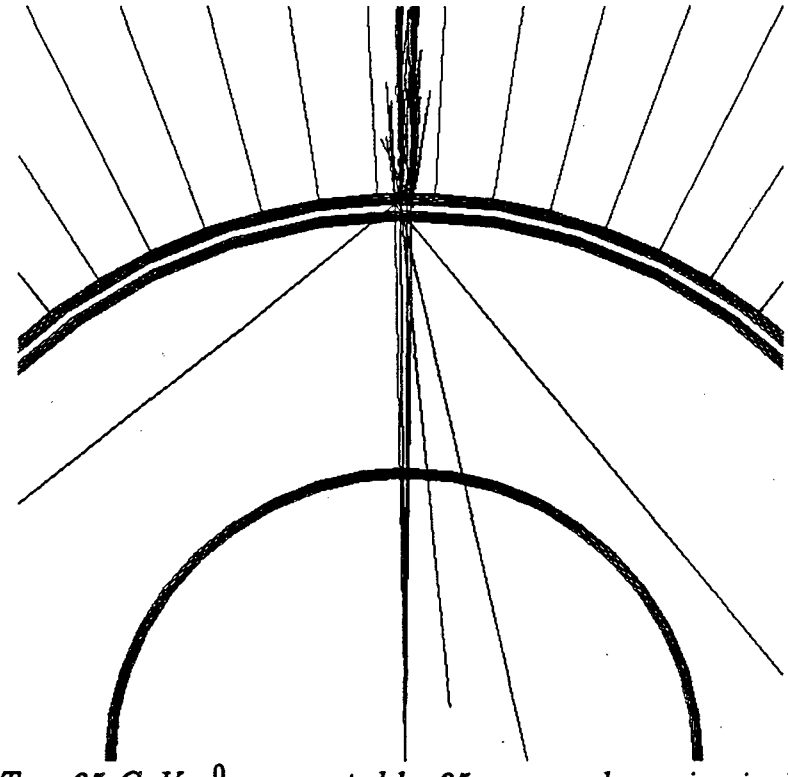

FIG. II.4 Two 25 GeV π^0s separated by 25 mr are shown impinging into one calorimeter cell. Pre-radiator system is shown.

Table II.4 Summary of $H \rightarrow \gamma + \gamma$ Requirements

Kinematics:		
	$\lvert\eta_\gamma\rvert < 1.5$	
	$P_{t,\gamma} > 20$ GeV	[or roughly $\frac{M_H}{4}$]
Resolution:		
	$\frac{\Delta E}{E} = 0.005 \oplus 0.07/\sqrt{E}$ [GeV]	
	σ[z-vertex] < 1 cm	
	σ[position] < 1 cm	
Backgrounds:		
	$\gamma + \gamma$	
	γ + j	[j$\rightarrow n\ \pi^0$]
	j + j	2 [j$\rightarrow n\ \pi^0$]
	cuts required:	
		isolation
		charged track veto
		$n\ \pi^0$ overlap> 1 cm
Trigger:		
	2 isolated clusters,	
	$E_t > 20$ GeV	rate 100 Hz

II.C $H \rightarrow ZZ^*$

The Higgs' mass range covered by this process is 130-160 GeV, and has also been examined previously[II.3-5]. The signal is one Z-boson and an additional di-lepton pair forming an off-shell Z-boson(Z^*). Large backgrounds consist of $t\bar{t}$ and $Z + b\bar{b}$ events, where the heavy quarks have decayed to leptons (e or μ). The intrinsic ZZ^* background is negligible. A mass requirement on one di-lepton pair identifies the real Z-boson. Isolation cuts reduce background to the Z^*, because at least two leptons from each source of background are non-isolated. The remaining event rate is small. Table II.5 gives a summary of a sample analysis.

For the mass range considered, the Higgs' width is narrow (< 1 GeV). Good resolution is necessary, but the requirements are less stringent than for the two-photon mode. Hence resolutions of $0.005 \oplus 0.07/\sqrt{E}$ for electrons and 0.11 for muons (angular dependences were included) were assumed. Figure II.5 shows the invariant mass spectra for the various modes. A summary of the ZZ^* requirements is given below.

Table II.5 ZZ^* Analysis Summary

Process	σ [pb] raw	Det. Cuts and	Phy. Cuts	σ [pb] final
$H \to ZZ^*$ M=140 GeV	$2.6 \cdot 10^{-2}$	$\lvert\eta_e\rvert < 1.5, \lvert\eta_\mu\rvert < 3$ $P_{t,e,\mu} > 10\ GeV$ $\Sigma E_t < 4\ GeV, R = 0.6^c$ $\Delta M_Z = 5[e], 10[\mu]\ GeV$ $20 < M_{Z^*} < 80\ GeV$		$3.3 \cdot 10^{-3}$
$t\bar{t}$	$3.2 \cdot 10^{2}$	"		$1.3 \cdot 10^{-4}$ [a]
$Z + b\bar{b}$	$3.5 \cdot 10^{0}$	"		$8.0 \cdot 10^{-5}$ [b]

[a] Isolation cut factor of 0.02 assumed. Number in 1% mass bin.
[b] Number in 1% mass bin.

[c] Isolation for e and μ for $|\eta| < 1.5$.

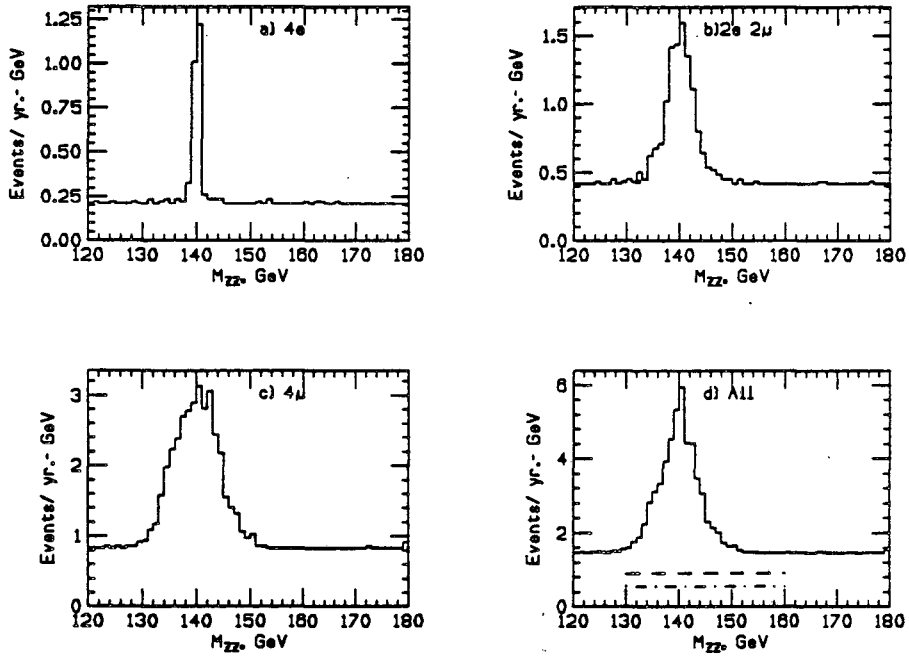

FIG. II.5 M_{ZZ^*} for 140 GeV Higgs plus $t\bar{t}$ and $Z + b\bar{b}$ backgrounds in (a)4e, (b)2e2μ, (c)4μ and (d) combined lepton modes ($t\bar{t}$ only in dashes and $Z + b\bar{b}$ only in dotdash) with ELMUD *resolutions. The estimated $t\bar{t}$ and $Z + b\bar{b}$ background are shown as a flat distribution and represent approximate level of expected background near peak.*

A Z-boson trigger should be sufficient for capturing the signal. The di-lepton trigger rate, including Z-bosons and heavy quarks, is expected to be over 10 Hz at

SSC design luminosity. A lepton trigger threshold of $P_t > 20\ GeV$ will suffice, and the two-photon trigger requirements will accommodate this channel.

Table II.6 Summary of $H \rightarrow Z + Z^*$ Requirements

Kinematics:			
	$\lvert\eta_e\rvert < 1.5, \lvert\eta_\mu\rvert < 3$		
	$P_{t,\text{lepton}} > 10$ GeV		
Resolution:			
	$\frac{\Delta E}{E} = 0.005 \oplus 0.07/\sqrt{E}$ [GeV]	for e	
	$\frac{\Delta P}{P} = < 0.11 \oplus 0.3 P_t$ [TeV]	for μ	
Backgrounds:			
	$t\bar{t}$	4 $[t \rightarrow e$ or $\mu]$	
	$Z + b\bar{b}$	2 e or μ + 2 $[b \rightarrow e$ or $\mu]$	
	cuts required:		
		1 Z, $\Delta M = \pm 10$ GeV	
		isolation	
Trigger:			
	2 isolated clusters,		
	$E_t > 20$ GeV	rate 100 Hz	(e)
	charged track	$\sim$ 10 Hz	(e or μ)

II.D $H \rightarrow ZZ$

The mass range covered is 160-800 GeV. This mode has been studied exhaustively [II.5-7] and nothing new is being added here. The reconstruction consists of finding two Z-bosons via four isolated leptons (e or μ). In addition the Z-bosons are moving with substantial P_t. Possible backgrounds are continuum-ZZ, $Z + jet$, $Z + t\bar{t}$, and $t\bar{t}$ events where the jet fluctuates to fake leptons or t quarks decay to leptons yielding a putative Z-pair. A tight Z-boson mass requirement, isolation cuts, and kinematic cuts, will reduce all backgrounds to low levels (even without track information or particle identification). Rates become small for the higher mass searches, so high lepton reconstruction efficiency is important.

Table II.7 ZZ Analysis Summary

Process	σ [pb] raw	Cuts	σ [pb] final
$H \rightarrow ZZ$	$2.4 \cdot 10^{-2}$	$\|\eta\| < 1.5[e], 3[\mu]$	$5.3 \cdot 10^{-3}$
$\rightarrow ee\mu\mu$		$P_{t,e,\mu} > 30\ GeV$	
M=400 GeV		$\Sigma E_t < 5\ GeV, R = 0.2$ [a]	
		$\Delta M_Z = 10[e], 20[\mu]\ GeV$	
		$370 < M_{ZZ} < 430\ GeV$	
$q\bar{q} \rightarrow ZZ$	$7.5 \cdot 10^{-2}$	"	$3.0 \cdot 10^{-4}$
$Z+$ jet	$1.4 \cdot 10^{2}$ [b]	"	$5 \cdot 10^{-4}$
$t\bar{t}$	$20 \cdot 10^{3}$ [c]	"	$< 1.5 \cdot 10^{-3}$ 90%CL

[a] Isolation applied on electrons only.

[b] Generator Cuts: $\sqrt{\hat{s}} > 350\ GeV$, $\hat{P}_{t,Z} > 45\ GeV$.

[c] No lepton branchings included.

The resolution requirements of heavy Higgs searches become modest as the mass and width become large. The lepton momentum resolution which yields a resolution of the reconstructed Higgs' peak equal to the natural width is roughly $M_H^2/2$. Thus a 0.45 TeV Higgs requires about 10% resolution.

The continuum Z-pair background is suppressed when Z-boson and lepton P_t cuts are applied. The other backgrounds giving fake Z-pairs, such as $Z + jet$, $t\bar{t}$, and $Z + t\bar{t}$, are all suppressed when lepton isolation and Z mass requirements are also used. Kinematic cuts such as these are almost all that are necessary. It should be pointed out that no electron identification was assumed in the analysis, only isolated EM clusters were used. Muon identification was assumed to be straightforward. The analysis is summarized Table II.8 and Figure II.6 shows invariant mass spectra for 200, 400 and 800 GeV Higgs.

A single Z-trigger will be sufficient for the ZZ mode as well. For Higgs' mass searches beyond 600 GeV, the event rates are low ($O(10)$). Although the signal to background is significant, larger integrated luminosities may be necessary. The muon system for ELMUD will be designed to be operational for luminosities of $10^{34} cm^{-2} s^{-1}$. The high rate triggering/readout capability of ELMUD of 100 Hz or better will *still* allow readout of all Z-bosons. For electrons, however, the issue of isolation cut viability needs to be studied. In studying a search for an 800 GeV Higgs, the kinematically acceptable ZZ events arising from $t\bar{t}$ decaying into three electrons plus one hadron is on the order of the signal [II.8], while contribution from continuum ZZ production is small. An isolation cut of $\Sigma E_t < 10\ GeV$ in $R = 0.2$ rejects the background and retains the signal. The calorimeter must function so that meaningful cuts can be made, then physics cuts at high luminosity, even for electrons, seem possible. Figure II.7 shows isolation cut acceptance for signal and background. Finally, the summary of detector requirements is given below.

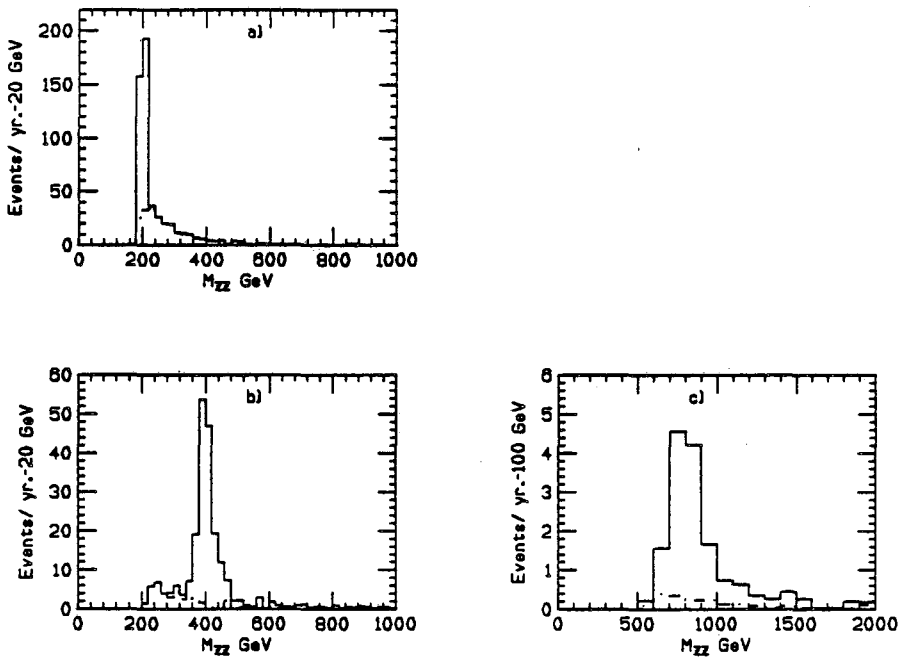

FIG. II.6 M_{ZZ} for Higgs decays to $4e, 2e2\mu$ and 4μ mode for Higgs masses of (a)200 GeV, (b)400 GeV, (c) 800 GeV with ELMUD *resolutions and cuts described in text.*

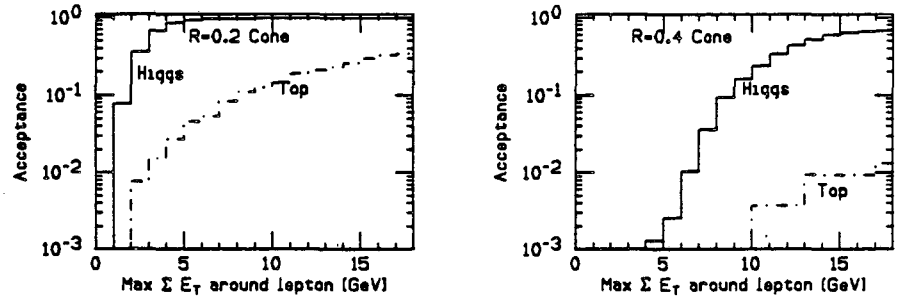

FIG. II.7 Very High luminosity Isolation Acceptance vs. ΣE_t around lepton for (a) $R = 0.2$ for 800 GeV Higgs events and top background, (b) $R = 0.4$ cone. For both plots, $< N_{interactions} >= 35$.

Table II.8 Summary of $H \rightarrow Z + Z$ Requirements

Kinematics:			
	$\|\eta_e\| < 1.5, \|\eta_\mu\| < 3$		
	$P_{t,\text{lep.}} >$	10,30,40, 60 GeV	
	$P_{t,Z} >$	10,60,140, 250 GeV	
	for $M_H =$	200,400,600,800 GeV	
Resolution:			
	$\frac{\Delta E}{E}$ required:	$\frac{M_H^2}{2}$ [TeV]	
		0.02, 0.07, 0.13,0.25	
Backgrounds:			
	$Z + Z$		
	$Z + t\bar{t}$	2 e or μ + 2 $[t \rightarrow e$ or $\mu]$	
	$t\bar{t}$	4 $[t \rightarrow e$ or $\mu]$	
	cuts required:		
		2 Z, $\Delta M = \pm 10$ GeV	
		isolation	
Trigger:			
	2 isolated clusters,		
	$E_t > 20$ GeV	rate 100 Hz	(e)
	charged track	~ 10 Hz	(e or μ)

II.E Summary

Higgs searches in the 2γ, ZZ^*andZZ decay modes have been studied. A detector based on what is necessary to perform such searches looks quite plausible. Good electromagnetic calorimetry and somewhat more modest muon momentum resolution are required. Kinematic cuts, Z mass constraints where relevant, and isolation cuts generally remove backgrounds to sufficient degree.

In the appendices (II.B-F) additional physics processes which yield final lepton or photon states are shown to have quite reasonable acceptance in ELMUD.

III. THE DETECTOR

III.A. Conceptual Design

The physical processes expected at the SSC and the detector requirements were described in Section II. Sensitivity to the minimal standard Higgs boson requires detection of muons, electrons, and photons over the decade from 0.1-1.0 TeV. It can be shown that this will enable the detector to study many other phenomena. The next sections summarize the detector performance, the design criteria, and cost estimates. The fundamental requirements are:

1. Muon resolution $\leq 10\%$
2. Muon efficiency $\geq 95\%$
3. $\pi^0\pi^0$ separation $\leq$1 cm
4. Electron photon resolution $= 0.5\%$
5. Electron photon efficiency $\geq 95\%$
6. Interaction vertex resolution $\leq$ 5 mm

In addition to these relatively objective requirements is the desire for simplicity and the notion of trying to make few and small technological extrapolations. For this conceptual design, fast elements are assumed. Scintillating fiber tracking and a dense calorimeter make up the central region and cover a cylinder out to $|\eta| = 1.5$. The muon system fills the outer volumes with an inner measuring layer, a toroid magnet, and two outer measurements. Since muon identification systems in the central rapidity region must reside outside the other detector components, they are generally large and can easily dominate the cost of a detector if very good resolution is desired. A set of simple exercises was performed to attain some insight into what constitutes a minimal size. The design presented here is not an optimization, but instead is an example.

The limit on the inner radius of the ELMUD calorimeter is the rate that can be sustained by the layers of scintillating fiber tracking that must reside inside. These fibers cannot be made too small, or there will be insufficient light for good efficiency. Assuming a fiber diameter of $750\mu m$ gives 4-5 photoelectrons per minimum ionizing particle and results in a 99% efficiency per fiber. The smallest radius the fiber tracker can be placed is based on the need to resolve separate tracks in the layer and to limit the number of false combinations in a super layer. A fiber tracker with 1.0% occupancy is better than 99% efficient at distinguishing two tracks and has a 25% false hit ratio. An occupancy of 1.0%, at a luminosity of $10^{33} cm^{-2} s^{-1}$, can be accomplished with $750\mu m$ fibers 40 cm from the beam. The outer radius of the tracker is set by the needed vertex resolution. With the outer layer of tracking at 50 cm, $750\mu m$ fibers, and ten degree stereo layers the vertex can be resolved to better than 5 mm using only one track, which meets our goal.

The calorimeter inner radius is 50 cm and extends to $z = \pm 100\ cm$. The largest angle a calorimeter cell can subtend in polar angle is constrained by isolation and trigger requirements. For isolation cuts it is necessary to impose a cone of radius $R = 0.2$ around the center of electromagnetic clusters. A cell size larger than 0.1×0.1 in $\Delta\eta \times \Delta\phi$ would not leave a zone of exclusion inside a $R = 0.2$ cone. In a projective geometry, a particle beginning at a point other than the origin can shower through more than one tower in η. In the trigger it would be difficult to distinguish any

particle showering in more than two cells in one dimension from a background jet. This implies that the minimum cell size in η must be 0.1 to keep all showers within two blocks in η, for a interaction that is two-σ away from the origin.

The polar angle segmentation is driven by different requirements. The calorimeter must provide sufficient position resolution to discriminate electrons from overlapping photons and pions and the cell size should be small enough to resolve close-together showers. Both of these requirements are met with cell sizes comparable to the shower width. In all of the media that will be considered the FWHM is a few cm, so 2.5 cm is used. At a radius of 50 cm from the beam this gives a cell with $\Delta\phi = 0.05$.

The calorimeter depth is set to be 27 radiation lengths so that leakage will not be a factor in resolution. The media considered all have radiation lengths of about 1 cm. This sets the outer calorimeter radius to 100 cm if electronics and access are included.

A natural muon system scale is perhaps more ill defined. For the heavier Higgs searches, the event rate will be limited. The luminosity requirements tend to be high so a muon system needs to be robust. The ZZ^* mode requires high resolution and the heavy Higgs requires modest resolution. Good resolution for low Higgs masses insures adequate resolution at high masses because resolution scales with momentum while the Higgs' width scales with the cube of its mass. The measured Higgs' width is dominated by lepton resolution when the lepton resolution is about $1/2 \cdot M_H^2$ where M_H is in TeV. Thus the measured width for 10% lepton resolution will dominate the natural width for a 450 GeV Higgs.

The muon system begins at a radius of 100 cm. First additional shielding is followed by the magnetic spectrometer. Iron toroids 3 m thick in the central region and 6 m in the forward were chosen for their combined cost and shielding advantages compared to other designs. This limits the resolution to (7-11)% due to multiple scattering. Increasing the thickness reduces the resolution only by the square root of the thickness while the amount of iron in the central region is increasing by the third power of its thickness. The amount of iron shown here balances the cost of the iron with the cost of the muon chambers. Different combinations, such as less iron in the central region and more in the forward, could improve the mass resolution for lower mass Higgs; however, optimization studies have not been performed.

Summary of Detector Requirements

This section presents in condensed form the motivation for the various ELMUD components:

ELMUD Design Criteria

Detector System	Item	Motivation
Pre-Radiator Tracker:	Fibre Length	Covers EM cal. region
	Fibre Diameter	Occupancy, z-vertex < 1 *cm*
	Number of Layers	z-vertex < 0.5 *cm*
	Radiator Thickness	$E_{absorbed} < 0.5\%$ for $H \rightarrow 2\gamma$
EM Calorimeter:	Resolution	$H \rightarrow 2\gamma$
	Inner Radius	e shower size, radiation damage
	η coverage	radiation damage
	Segmentation	Shower Size, Isolation and trigger tower
Muon System:	Absorber Thickness	Chamber Hit Rate
	Iron Thickness	Multiple scatter.
	Inner Radius	Size of EMC and absorber.
	η coverage	Decay μ rate
	Chamber size	Occupancy at 10^{34} and trigger

III.B Tracking

The physics goals of ELMUD require tracking information to determine the z-coordinate of the vertex from the triggering interaction and calorimeter impact points for particle identification. Track segments before the calorimeter can also provide redundant information to aid muon momentum measurements. The inclusion of a radiator will enable the device to locate and to some extent identify electrons, photons, and π^0s.

The granularity of this device need not be especially fine because only straight tracks will be reconstructed; however, the occupancy must be kept low to avoid pattern recognition ambiguities. Since some tracks will eventually be matched to the calorimeter, the $r-\phi$ resolution should be comparable to that obtainable from the shower centroid which is a better than 1 mm. The necessary z-position resolution is determined by requirements of interaction vertex measurements (≤ 1 cm) and to a lesser extent by calorimeter matching.

Because of its intrinsic speed and moderate resolution, plastic scintillating fibers(PSF) are well matched to the task. With careful choice of fibers, sufficient radiation hardness can be obtained. Polystyrene based ternary scintillators(3HF) emit light in the yellow-green portion of the spectrum[III.B.1]. Since radiation damage is most severe in the UV region, it will not be a problem for trackers in the central rapidity region[III.B.2]. To get the light out of the detector to photon counting devices, undoped polystyrene fibers would be welded to the doped fibers and routed to the outer portions of the detector. Undoped polystyrene fibers have an attenuation minimum at 550 nm and are well matched. Finally, the readout devices of choice for SSC experiments are all silicon based and have high (60%) quantum efficiency in the yellow-green wavelength range. PSF fibers 750μm in diameter yield 3-4 photoelectrons for each minimum ionizing particle after attenuation by 100 cm of fiber. If the fibers are used in doublets offset by 1/2 a fiber diameter and 10% dead area assumed between fibers, then the single charged track efficiency for a doublet ranges between 98-99%.

The initial design covers the central rapidity region with two 1 m fibers read out at each end of the chamber. The geometry of the proposed tracker is shown in Figure III.B.1. The extent along the beam is $\pm$ 100 cm and is matched to the calorimeter coverage. Preliminary studies have focused on a design with three superlayers in each half of the detector. Each superlayer is consists of two axial and two stereo layers made from 750μm fibers. Each layer is offset by 1/2 a fiber diameter to eliminate the dead area between fibers and give an effective resolution of 1/2 a fiber diameter. The first superlayer starts at a radius of 40 cm. The second and third superlayers sandwich a tungsten radiator and would be mounted as close to the calorimeter as possible to give an impact position with a small lever arm and to minimize spreading of showers that initiate in the radiator.

The critical issue in the use of short PSF is the type of readout that will be used. To date the only successful use of PSF in experiments has been with CCD readouts which are much too slow for SSC applications. One of the most promising developments in readout devices is the miniaturization of Avalanche Photodiodes(APD). In the near future these devices will be available mounted 8/chip[III.B.3], which is close to the desired degree of compactness and it is likely that larger packing fractions will soon be available. Our design uses APDs operating in proportional mode to enable individual bunch crossings to be resolved. Operation

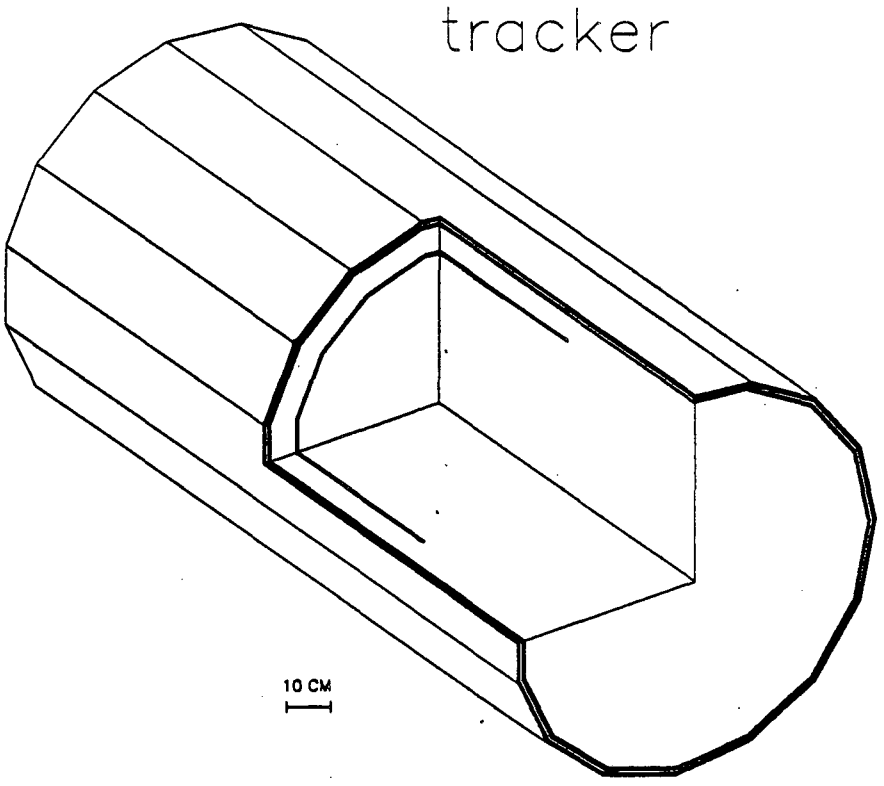

Figure III.B.1 ELMUD *Tracker*

in this mode requires pre-amps and has a significant signal to noise ratio[III.B.4]. Detailed pattern recognition studies will be necessary to determine the necessary degree of redundancy that is necessary for high tracking efficiency. Because of its apparent ease of operation, low cost, and simplicity, use of APDs in Geiger mode should also be investigated.

Another interesting development in readout devices are visible light photon counters(VLPC), which are a variant of solid state photomultipliers (SSPM). These devices are most sensitive to the IR part of the spectrum. Tests with 0.5 mm 3HF[III.B.4] fibers have demonstrated a mean of five photoelectrons per minimum ionizing particle(MIP). It should be noted that VLPCs operate at seven degrees Kelvin and therefore require a cryostat outside the detector.

The z-vertex resolution(σ_v) is given by

$$\sigma_v = \frac{1}{\sqrt{N}} \times \frac{w}{\sqrt{12 tan\alpha}} \times (2\frac{R_c}{\Delta R} - 1)$$

where w is the fiber diameter, α is the stereo pitch, R_c is the calorimeter inner radius, ΔR is the distance between the layers, and N is the number of tracks. With R_c = 50 cm, $750\mu m$ fibers, ten degree stereo, $w = 750\mu m$, and one particle, σ_v = 0.5 cm which was the goal. Figure III.B.2a shows the simulated resolution obtained using the 4 lepton tracks from $H \rightarrow ZZ \rightarrow ee\mu\mu$. Figure III.B.2.b shows the resolution using all tracks in the event. Figures III.B.2.c-d show the resolution at luminosities of $10^{33} cm^{-2} sec^{-1}$ and $10^{34} cm^{-2} sec^{-1}$ respectively. In these plots the average of all

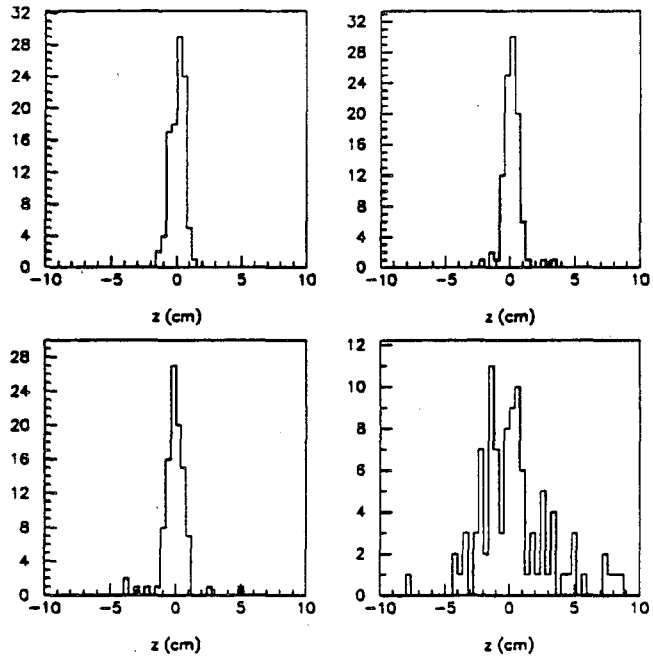

Figure III.B.2 Vertex resolution : (a) four leptons only, (b) full event, (c) full event and pileup for $10^{33} cm^{-2} sec^{-1}$, *(d) full event and pileup for* $10^{34} cm^{-2} sec^{-1}$.

the impact points in the event were used. The best resolution is obtained using only large angle tracks. At high luminosity the resolution is severly degraded so it would be necessary to use only the trigger leptons. This is not seen as a serious problem because at high luminosity the resolution requirements are not as stringent.

Some preliminary pattern recognition studies have been undertaken to understand the problems to be expected at higher luminosity. Single superlayers were simulated for a range of luminosities from $10^{33-34} cm^{-2} sec^{-1}$. Figure II.B.3 shows that the configuration can rapidly become superefficient, or find more tracks than really exist, as higher luminosities are approached. The cause of the extra hits are ambiguities from close-together tracks that are not resolved by stereo layers. The configuration simulated was for $750 \mu m$ overlapped fibers with ten degree stereo layers at several different distances from the interaction using only particles with $|\eta| \leq 1.5$. It is clear from this figure that pattern recognition could be problematic at high luminosity for small radii layers. It should be pointed out that no attempt was made to further disentangle ambiguities by using information from other superlayers. Also the implications for electron identification and charged track isolation have not been studied thus far.

The effect of the stereo angle was also studied as a function of the superefficiency and z-coordinate resolution. These plots are shown in figures II.B.4-5. The z-coordinate resolution is not improved by stereo angles much greater than ten degrees; however, the superefficiency of configuration increases with stereo angle as expected.

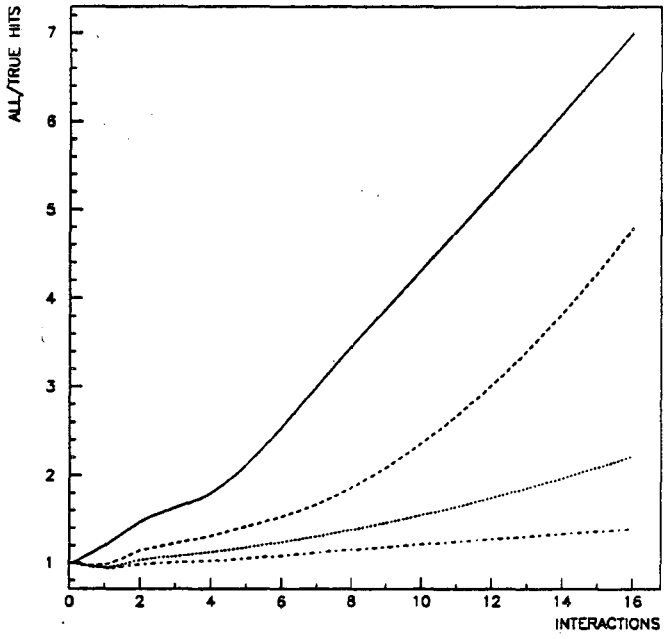

Figure III.B.3 Efficiency versus the number of interactions per bunch crossing for: 25 cm(solid), 50 cm(dashed), 100 cm(dots), 200 cm(dot-dash).

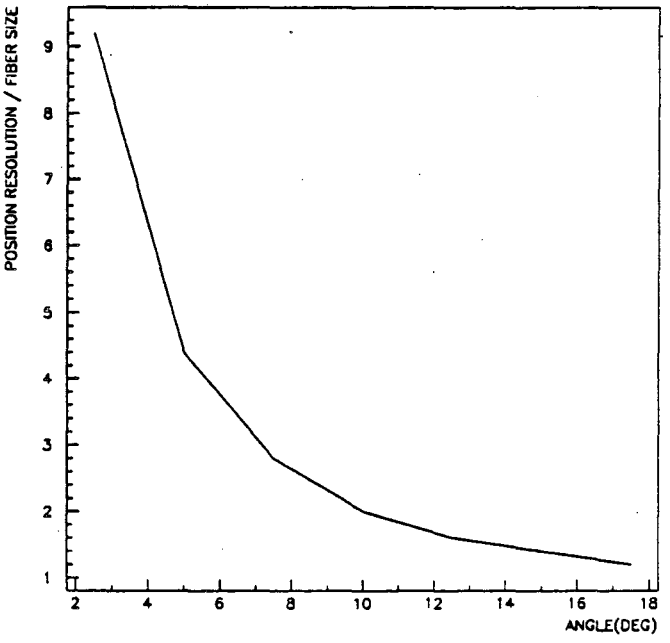

Figure III.B.4 z-coordinate normalized to the fiber diameter vs stereo angle.

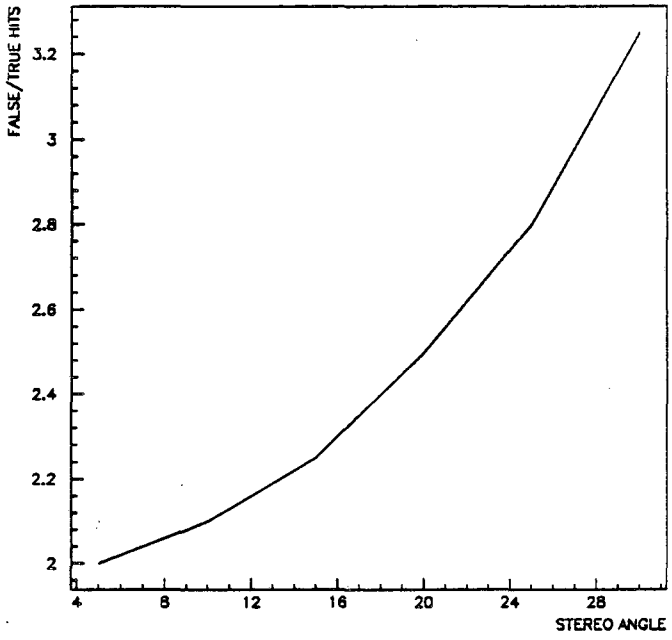

Figure III.B.5 Efficiency vs stereo angle for 750μm fibers 25 cm from the interaction.

A high-Z radiator has been included in the design to aid in particle identification. A 7 mm cylindrical shell of tungsten was chosen for the radiator because it is not radioactive and has a 20:1 ratio of hadronic interaction length to radiation length. This makes the radiator essentially transparent to hadrons while the two radiation lengths have a photon conversion efficiency of 80% and degrade the calorimeter resolution by less that 0.2%.

The tracker pre-radiator combination can provide excellent electron identification which is independent of the calorimeter. Figure III.B.6 shows the energy distributions in the fiber layer after the radiator produced by charged pions and electrons. A cut of 1.5 MIPs yields an electron efficiency of 96% while rejecting 94% of all the hadrons. While this discrimination is impressive it implies the use of ADCs on each fiber which would be a very expensive option. Another option is to count the number of hit fibers using the rough proportionality of hits to energy as the discriminant. Figure III.B.7 shows the hit multiplicity distributions for different particle species. A cut at 2 MIPs has a 92% electron efficiency with 91% hadron rejection. This rejection could be improved by optimal placement of the radiator with respect to the outer fiber layer to allow the initiated showers to spread and hit more fibers; however, the effect of the higher occupancy on pattern recognition needs to be studied. The factor of ten in e/π separation that is obtained in the prototype configuration is an independent discriminant that is multiplicative with track matching and lateral shower shape requirements.

A pre-radiator with sufficient position resolution can measure the single and collimated multiple π^0 events directly in the experiment. A 50 GeV π^0 has a minimum

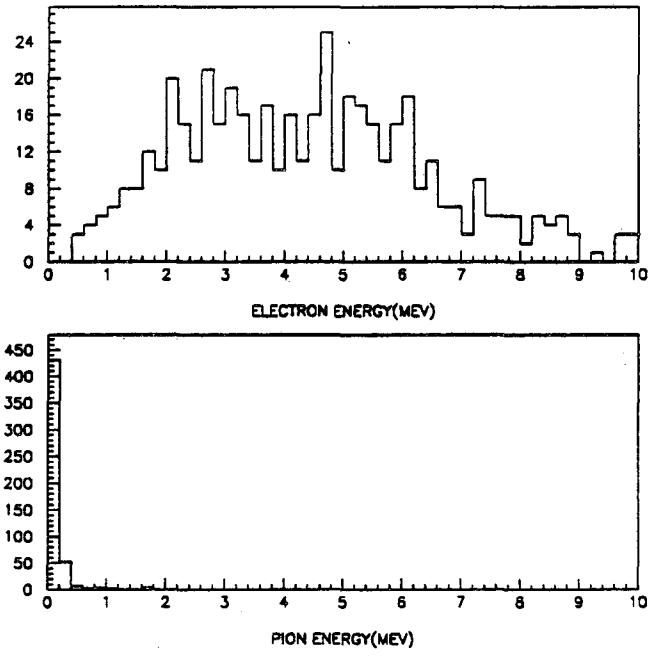

Figure III.B.6 Pre-radiator energy distribution

opening angle of 2.5 mm which is large enough to be resolved as two distinct clusters; the number of hits is shown in Fig.III.B.7. The background of single π^0 or collimated multiple π^0s may therefore be checked directly, and the pre-radiator information used to reject events with some loss of efficiency.

Tracking pads are added to the tracking system to resolve ghosts, to provide a low channel count multiplicity trigger sum, and to provide un-ambiguous fast information on the charged particles entering a calorimeter tower, both before and after the pre-radiator. Each pad is composed of a scintillating tile, 5 mm thick, read-out by a wave-shifting fiber inserted in a groove, in the manner proposed by SDC EOI/LOI for calorimeter readout. One MIP crossing a pad will give about 10 p.e. with a 60% quantum efficiency photocathode, as in the Si-based fiber read-outs. The size of the pads is matched to the calorimeter cell size of 0.05×0.1, giving 4K pads/layer. Two layers in the tracker and one layer in the pre-radiator would yield 12K channels. A fast comparison between the corresponding pre-radiator pad(s) and calorimeter tower would give a fast trigger for a photon or electron, when combined with the calorimeter information.

The total channel count for three superlayers is 94 k. With 1-bit readout accuracy this means that 12 kbyes of data are read out for each trigger. The cost of the detector is based on estimates by the EMPACT[III.B.5] collaboration scaled on a per-channel basis to ELMUD. The fibers and support structures are then about \$17/channel. The cost of signal handling assumes APDs run in proportional mode. APDs, preamps, discriminators, and analog pipelines with power supplies and cables included are \$67/channel. The 8K scintillating pads are estimated to cost about \$100/channel. The total cost for is then about \$9M.

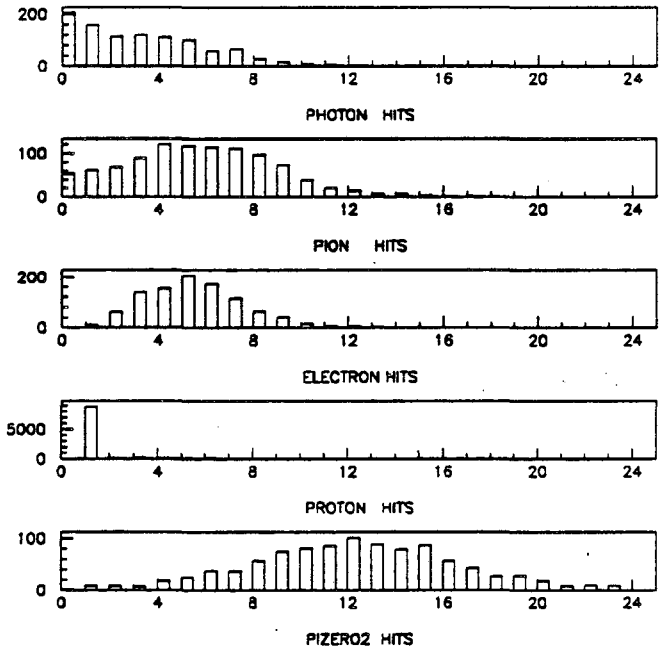

Figure III.B.7 *Hit multiplicity distributions in the fiber layer after the radiator for: γ, π^0, e, p, and $2\pi^0$s(separated by 1 cm).*

III.C Calorimeter

The calorimeter in ELMUD is a relatively modest device that covers the angular region $|\eta| \leq 1.5$. This angular coverage is sufficient to double the acceptance for high-mass Higgs' searches compared to a device that detects only muons. Since calorimeters have better resolution than muon detectors at high energies, it gives the detector sensitivity to narrow high-mass states decaying to electrons, e.g. Z-bosons. If calibrated well (1/2%), it will offer the unique opportunity to see the intermediate mass Higgs via its decay to two photons. This design uses an electromagnetic calorimeter of a depth sufficient to fully contain electromagnetic showers and to make crude energy measurements of jets. About 1/2 of all hadronic energy is deposited in the first absorption length, so jet counting and isolation can be implemented. Figure III.C.1 shows a schematic of the calorimeter. The purpose of the ELMUD calorimeter is to measure electrons and photons only; therefore, the integration time is not driven by compensation requirements and can be made as small as possible. Another advantage to having only an EM calorimeter is that it can be supported from the ends in compression. Since no missing energy measurement will be attempted the dead areas used for these support structures are not important.

Since the detector covers only the central rapidity region it is perfectly matched to the cylindrical symmetry of hadronic collisions. The backgrounds from minimum bias events in the same bunch crossing are uniformly distributed in pseudorapidity (η). The cylindrical design of the calorimeter with constant η segmentation allows for calorimeter towers which present the same physics and physical size to a shower.

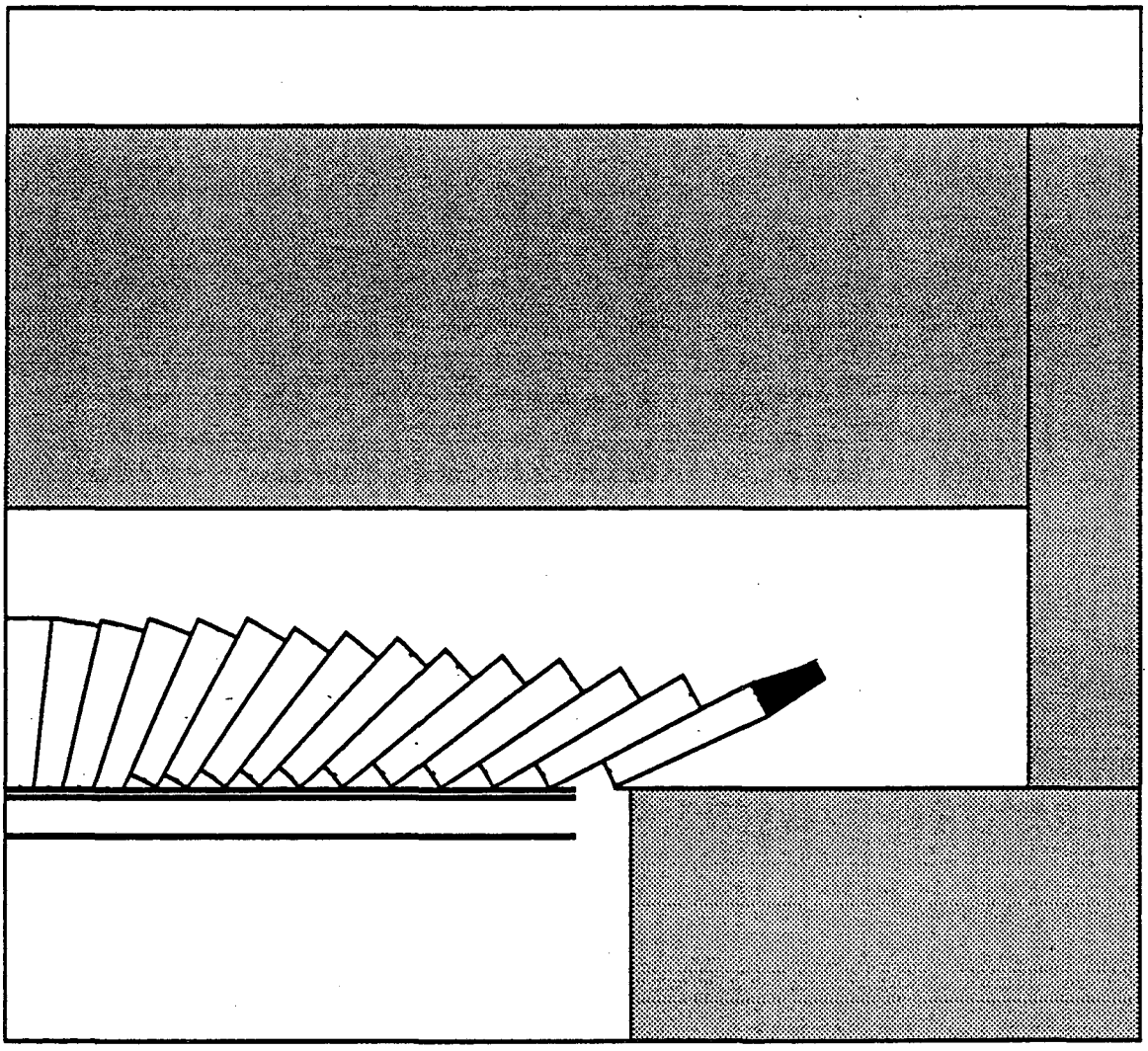

Figure III.C.1 ELMUD *Calorimeter*

This has the advantage of making an isolation cut an invariant quantity across the detector since the lateral shower size increases slowly with energy. The degree of segmentation is chosen to be 0.1×0.05 in $\eta - \phi$ units. The η segmentation is dictated by the smearing of the interaction region which has $\sigma = 7$ cm; segmentation of 0.1 allows particles from two-σ beam interactions to cross at most two towers. This can be pictured using figure III.C.1.

In ELMUD the ability to do isolation cuts and resolve showers that are close together is of paramount importance and determines what is an acceptable inner radius. To a large extent this depends on the calorimetric medium chosen since this influences the shower size. For example, Figure III.C.2 shows the simulated[III.C.9,10]radial escape curve for a calorimeter made from a 1:1 volumetric mixture of lead and scintillating fibers. A cylinder of radius 1.0 cm contains 63% of the energy for 100 GeV electrons. In the ϕ-dimension, that is not affected by interaction region smearing, the shower would be mostly contained in one or two 2.5 cm towers, which would allow

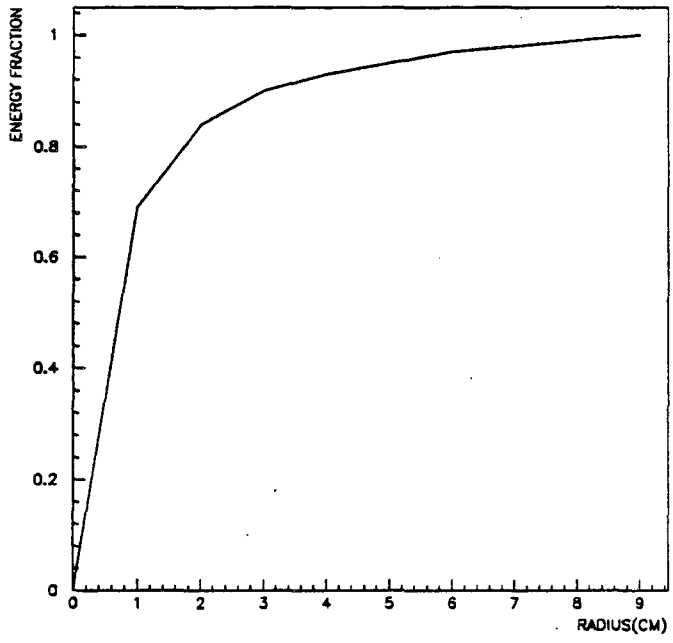

Figure III.C.2 Radial escape curve for 100 GeV electrons in a 1:1 PSF/Pb calorimeter.

neighboring cells to be examined for shower shape consistency which is equivalent to isolation.

It can be shown that the tower dimension(D) is related to position determination by[II.C.12]

$$\sigma/Rb = \sqrt{4b/D(e^{D/2b} - 1) - 1.}$$

where R is the energy resolution and b is the 1/e length of the shower. This function is plotted in figure III.C.3. The projected radius of a shower(b) is about 1.4 cm. This will give position resolution better than 1 mm for energies of interest and is well matched to the tracking detector. Charged track matching with calorimeter impact points and lateral shower shape measurement are two of the particle identification methods that will be used.

The most interesting signals at the SSC will involve isolated leptons. Pileup degrades the measurement of isolation, so any proposed system should be capable of resolving single bunch crossings. The calorimeter must also be radiation hard, compact, and capable of good resolution. Several options show the potential of satisfying all of these requirements.

Lead scintillating fiber calorimeters with a 1:1 ratio are inexpensive and, if electromagnetic signals only are of interest, can resolve individual bunch crossings. The resolution of such a device has been shown[III.C.2] to be $7\%/\sqrt{E}$ and, with the correct choice of fibers, can withstand the radiation doses expected at the SSC for several years. The dose at $|\eta| = 1.5$ was calculated to be 0.6 Mrads for 4 years($4 \times 10^7 sec$) at luminosity $10^{33} cm^{-2} sec^{-1}$[III.C.3]. Data from the JETSET collaboration[III.C.2]

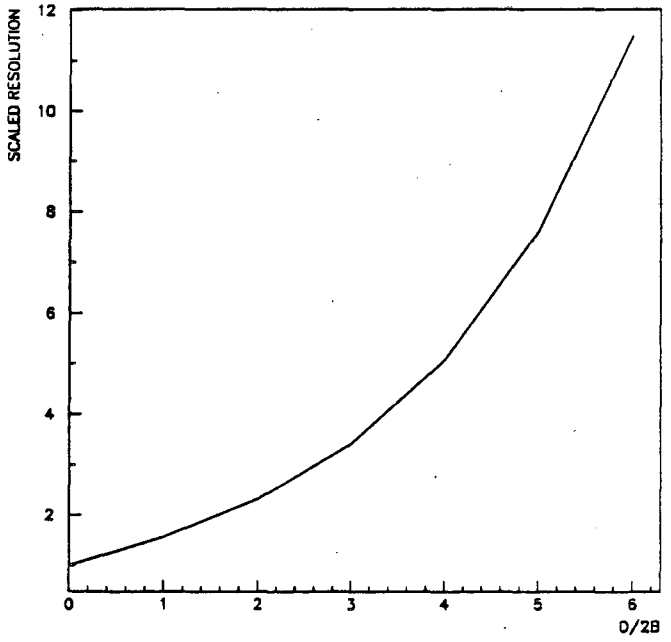

Figure III.C.3 Normalized position resolution versus normalized tower size.

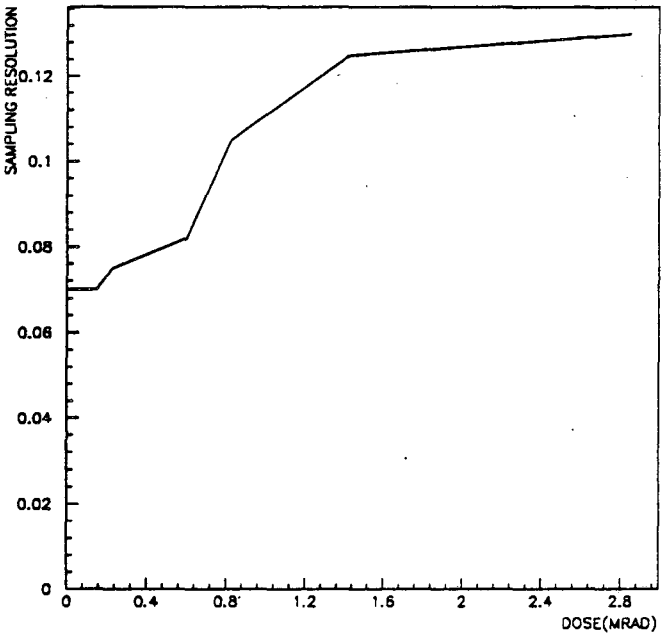

Figure III.C.4 Resolution versus Dose for a JETSET calorimeter module.

is shown in Fig III.C.4 which demonstrate the excellent sampling resolution obtainable. The measurements were made at low energies and therefore do not accurately measure the position dependent signal variations that have been measured by other

tests[III.C.4]. It is necessary to use a pre-radiator to initiate showers before entering the calorimeter to reduce systematic effects resulting from the impact point variations. Also, by incorporating non-pointing(in ϕ) fibers within the context of projective modules the effect can be further minimized.

Another very interesting option is lead fluoride which is a Cherenkov radiator with a radiation length of about 1 cm[II.C.5]. A small amount of light is produced by low energy lateral tails which makes the showers more compact than other media with comparable Moliere radius(R_M). PbF_2 has been shown to be 500 times more radiation resistant that SF-2 Lead Glass[II.C.6] and responds well to bleaching with UV light. It has been speculated that with sufficiently pure raw materials that PbF_2 could have the same radiation hardness properties as BaF_2. The resolution is limited by photon statistics to 3% $/\sqrt{E}$. With careful attention to light collection, lead glass calorimeters have been calibrated to 0.5% [II.C.7]. The technology of PbF_2 is very new and requires vigorous research and development before it will be useful as a calorometric medium; however, the technology is similar to BaF_2 and could be developed in time for SSC experiments with short lead times.

New levels of precision calibration will be necessary to study the two-photon decay of the Higgs'. Short term relative calibration is achieved by taking advantage of the symmetry of the detector's response to minimum bias events by demanding that the energy deposition be constant in ϕ and smoothly varying in η and equal for both ends of the calorimeter. Precision light injection has achieved a calibration of less than 0.5% over the long term in large calorimeter systems (CLEO). In ELMUD, a sub-ns laser would be mode-locked to the accelerator RF, and injected through optical fibers at beam crossing time during calibration acquisition runs. Cavity-tuneable UV-visible light can be injected selectively in the front and in the rear of the calorimeter towers to independently measure scintillation and transmission radiation damage, calorimeter stability, and photodetector response. Sufficiently stable quartz optical fibers exist for this purpose.

When a calorimeter is calibrated in situ, the beam is usually steered so that it is aimed at one calorimeter cell. Most calorimeters have cells that will not fully contain a shower so a procedure which minimizes the resolution by variation of the calibration constants is used. To set the absolute scale, the beam energy must be known to the desired degree of accuracy. In ELMUD, a 'beam' of Z-bosons will be used since each calorimeter cell will be hit by about 300 electrons from Z-boson decays during one year of running. An iterative process, using one cell as the target for calibration while all other cells use the n-1'th iteration of constants, would be used to set the absolute scale. If position dependent responses can be controlled, then this would allow calibration to the desired degree.

Photo-detectors of sufficient linearity, gain, and dynamic range for SSC calorimetry are under development, but are not yet standard items for research. The dynamic range is required to be from about 0.1 MIP (50 MeV) to 2 TeV, a dynamic range of 4×10^4, for SSC EM calorimeters, an extreme feat. This linearity is available only with Hybrid PMT if a photoelectron gain of 2,000 or more is required. In this device, a solid state diode replaces the dynodes, using the EBS gain mechanism. Hybrid PMTs have recently been tested with success by the LAA project at CERN.

Sampling calorimeters made with high-Z absorbers and argon are known to have excellent linearity and are easy to calibrate. With sufficiently fine sampling they can have resolutions better than 10% $/\sqrt{E}$. Attention has recently been devoted

to shortening the ion collection time by addition of dopants like methane. The use of solid argon also has the possibility of shortening ion collection times[II.C.8]. In addition, much work has gone into engineering studies[II.C.9] of how to construct liquid argon calorimeters with very small amounts of internal dead areas. Also one could rely on multilayer board technology which minimizes the space between towers by moving the connections from the sides to the back of each module. Since this is such a well established technology, its use should not be ruled out at this stage.

A post-radiator may be necessary to tag hadrons and fake electromagnetic events where large apparent EM energy is seen in the calorimeter, but which are the result of Kaons, or pion/gamma overlaps missed by the pre-radiator, or pion charge exchange partway down the calorimeter. Essentially, it is a spatially crude pre-radiator placed after the 30 radiation length electromagnetic calorimeter, before the hadron absorber. It consists of three layers of a scintillating tile/pad system similar to that in the pre-radiator, interspersed with two layers of 1-2 radiation length sheets of Pb. The pads have the same segmentation as the calorimeter, giving about 12K channels. Each fiber readout is digitized by 8 fast comparators, set at, say 0.5, 1, 2, 3, 5, 10 , 25, and 50 MIPS, encoded into a three bit number (4.5K packed data). The exact threshold settings would be determined so that a fast veto could be sent to the electromagnetic trigger. The expected performance of such a post-radiator has not been checked.

In summary, the fast electromagnetic part of ELMUD consists of a tower of tracker pads, a tower EM calorimeter, and perhaps a tower of post-radiator, all covering the same $\eta - \phi$ trigger cell. The signals from all tower signals are combined at the level one or two triggers for QCD jet discrimination.

To estimate the cost of the Pb-Scintillator calorimeter estimates from the EMPACT LoI were scaled either by volume or channel where appropriate. We use \$1750/channel for calorimeter module construction and all signal handling. For 3770 channels the full calorimeter is estimated to cost \$6.6M.

III.D Muon Spectrometer

A robust SSC muon detector should be able to run at the highest luminosity over almost the entire solid angle with good particle identification and momentum resolution. The muon detector complements the electron calorimeter in a variety of ways. Particle identification is more straightforward but the resolution is not as good. Due to being behind absorber, radiation does not limit detector performance in the higher rapidity region. The limit on angular coverage is then predominantly limited by being able to trigger. The ELMUD design, with an electromagnetic calorimeter for $|\eta| < 1.5$ only, allows the absorber shielding in the forward region to be optimized for muon triggering and identification. This allows ELMUD to increase the muon coverage to $|\eta| = 3$.

Because muon systems are usually outside all other detectors, they fill and instrument large volumes and therefore can be very expensive and easily dominate the cost of an entire detector. Indeed muon systems reach a point of diminishing returns very quickly so it is important to estimate what resolution is really acceptable. In addition to the resolution goals, another main determining factor on the cost of a muon system is the inner radius at which it begins. It will be shown that ELMUD has considerable leverage on cost/performance because of its small inner radius. One also wants to attempt to cost-optimize the muon detector layout for the physics processes of interest. As a simple approximation, muons are produced flat in rapidity up to the kinematic limit for a particular channel with underlying high mass states having a more central distribution. This, combined with phase space factors, leads to the forward region having the highest density of muons per detector area even for states with masses near 1 TeV. If uniform resolution versus P_t is normalized to the muon density, then the muon detector at 90 degrees is most expensive.

Designs using air-gap magnets tend to have excellent resolution for lower momentum muons; however, the limited amount of absorbing material makes muon identification more difficult and the rates higher. Conventional iron toroids have more than enough absorber but have their resolution limited by multiple scattering. An alternative is to use super-ferric magnets. One then has the benefit of iron in terms of its magnetization, its hadron absorbing power, and its use as a support structure but with the added possibility of reducing the contribution of multiple scattering to the muon momentum resolution. The disadvantage of a super-ferric magnet is the cost of the coil and cryostat.

For the central region, one can consider using either a normal iron toroid, an iron solenoid, or a super-ferric solenoid (such as in the Juné 1990 "10^{34}" EOI). For a solenoid, the vertex point is known and can always be used in determining the muon momentum. However, the contribution to the resolution from multiple scattering increases in a solenoid as the incident angle decreases as opposed to decreasing for a toroid. For example, if the two geometries had the same thickness, the resolution for the solenoid would be 40% larger for muons incident at 45 degrees. Also, in a solenoid, the flux needs to be returned and the field in the central and forward regions are perpendicular. These tend to produce awkward configurations in the transition region (or forward magnets at larger distances from the interaction point). Cost considerations have dictated using conventional, 3 m thick iron toroids in the central region for the prototype design. This gives a momentum resolution of about 10% at 90 degrees.

For the forward region, 6 m thick normal iron toroids are adequate. This lowers the contribution due to multiple scattering to 7% while also providing additional shielding in the high rate region. In principle, a super-ferric design in the forward region might be an interesting candidate. It is a relatively small magnet that would cover an appreciable solid angle; therefore, it might be cost effective and is further discussed below.

III.D.1 Design

Figure III.D.1 shows a layout of the proposed muon spectrometer. Table III.D.1 summarizes key features of the muon system.

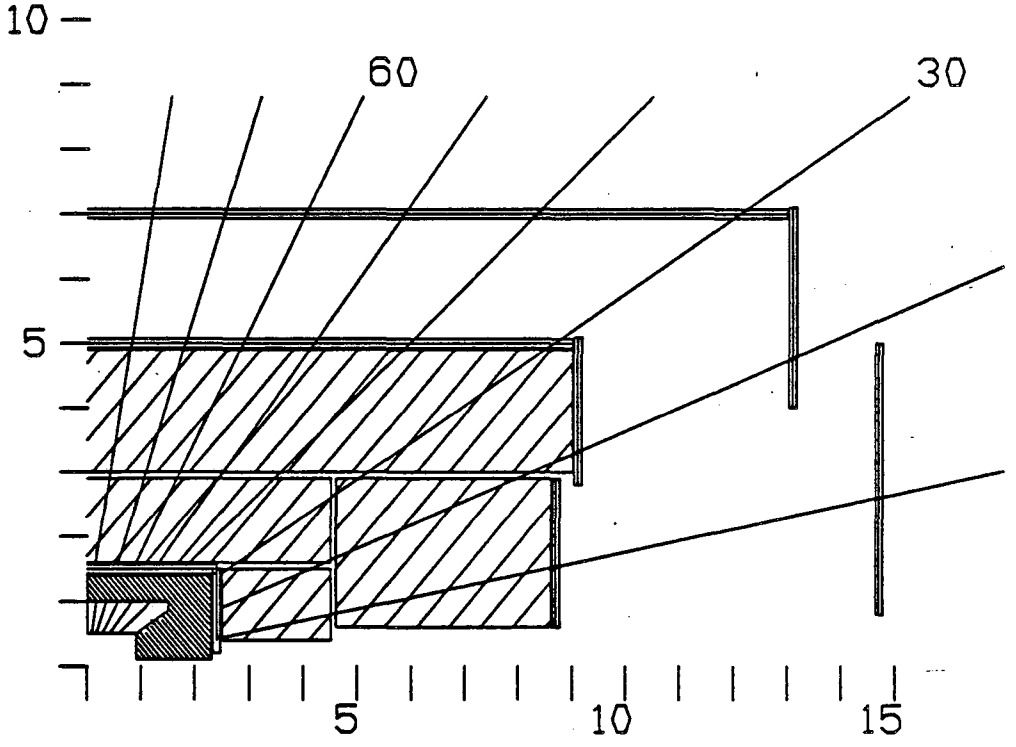

Figure III.D.1 ELMUD *muon system using normal iron toroids.*

The central toroid is divided into two contiguous boxes for a total thickness at 90 degrees of 3.3 m. For now, a measurement layer between the two boxes is omitted; such a layer may be needed for added redundancy and will be considered below. The central toroid is a hollow box with cylindrical forward magnets placed inside. This naturally gives space in the corners to service those detector elements inside the muon system. For the forward toroids, two separate magnets are assumed with a total thickness of 6 m with a measurement plane separating them. The relative amount of iron in the central and forward regions has not been optimized; a detector which is somewhat thinner at 90 degrees and thicker in the forward region could improve the performance in channels such as $H \rightarrow ZZ^*$.

Table III.D.1 : ELMUD Muon System

	Central	Forward
coil	normal	normal
geometry	2 boxes	2 cylinders
inner radius	1.6 - 2.9 m	0.4 - 0.6 m
outer radius	2.9 - 4.9 m	1.6 - 2.8 m
length	9.0 - 18.0 m	2.0 - 4.0 m
B_i (iron)	2.0 T	2.0 T
weight (total)	9600 mt	1800 mt

In order to reduce the punchthrough rates from the majority of hadrons from an event, absorber will be placed before the initial muon chambers. In the central region, an additional 3-5 λ of material behind the 1 λ calorimeter is estimated to be sufficient. To minimize the space and the number of radiation lengths, copper appears to be a good choice with 50 cm giving 3.5 λ and 35 X_0. In the forward region, the hadrons have higher momentum and more absorber is needed; however, albedo creating hits in the tracker and calorimeter needs to be carefully considered. For now 1.3 m of space is assumed to be available. Using copper would give 9 λ and 90 X_0. An alternative design would use 30 cm of tungsten followed by 1 m of copper giving 10 λ and 160 X_0. The tungsten in the first few absorption lengths would minimize the amount of hadronic punchthrough as this is roughly dependent on the density.

The geometry and technology used to measure muon trajectories will vary between different regions. For the regions outside the iron, the area covered is similar to the DØ muon system and this type of chamber is used as an initial design[III.D.1]. As will be discussed below, considerations of the trigger lead to cell sizes of 10 cm for $|\eta| < 1.5$, 5 cm for $1.5 < |\eta| < 2.5$, and 1 cm for $|\eta| > 2.5$. Inside the iron, the rates will be larger and so cell sizes of about 5 cm, 1 cm, and 0.5 cm will be needed. These could still be drift cells though it may be advantageous to use scintillating fibers or MWPCs for the higher angle region.

Trigger counters will also be needed. The geometry and design of these counters is similar to that presented in the DØ upgrade proposal[III.D.1]. In the central region, a single layer of counters is used to both tag the bunch crossing and initiate the muon data acquisition. In the forward region, the rates are higher and either two or three layers of counters, probably in a tile geometry, would be used in conjunction with the drift chambers to form an initial muon trigger able to make a P_t cut at about 20 GeV/c.

III.D.2 Resolution

The muon momentum resolution depends on two factors: multiple Coulomb scattering (MCS) and the position resolution of the tracking devices. The multiple scattering for iron toroids and a 2 T field is $0.18/\sqrt{L_{mag}}$, where L_{mag} is the length of field region. In the central iron box, the geometry produces a ϕ dependence which worsens the resolution by a factor of 1.04 on average. For the 3 m thick central toroid

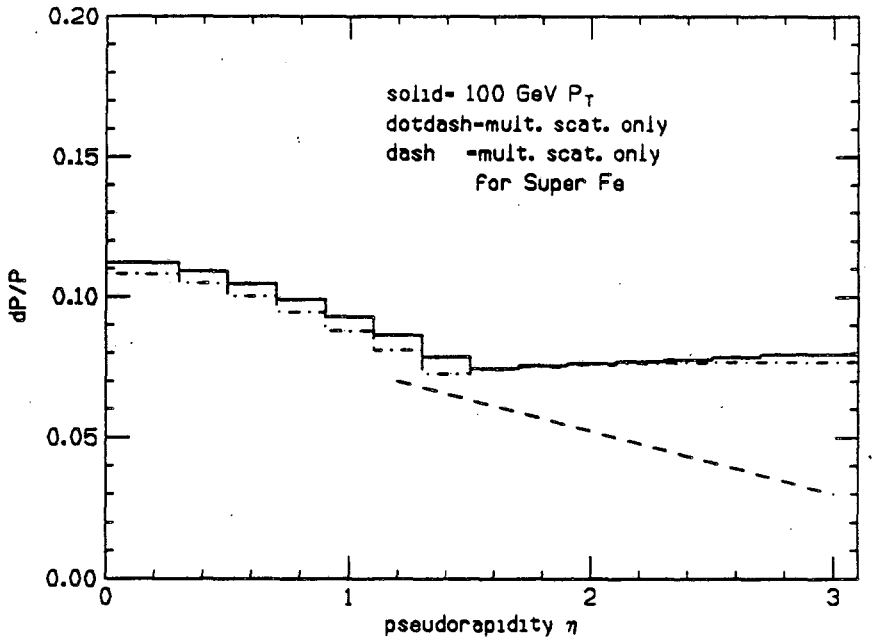

Figure III.D.2 The dP/P versus pseudorapidity for a 100 GeV P_t muon in ELMUD *(solid includes measurement and multiple scattering, dotdash shows multiple scattering only and dash is with a super-ferric forward toroid).*

and the 6 m thick forward toroid system, 11% resolution at $\eta = 0$ and 7% at $|\eta| = 3$ is expected. Figure III.D.2 shows the multiple coulomb scattering contribution to resolution versus rapidity. It also shows the resolution assuming a 2 m thick, 4 T super-ferric magnet in the forward region.

The other contributing factor to the momentum resolution is how well the trajectory of the track is measured. This dominates at the higher momentum. Simplistically, five points are measured for each muon: the vertex (from other tracks in the event), entering the calorimeter, before the toroid, immediately after the toroid, and at the maximum extent of the detector. At higher luminosities, the vertex will not be determined and there will also be some degradation in the ability to use the information in the PSF tracker. For large iron spectrometers such as ELMUD, position uncertainty will be dominated by alignment errors. For now, a position resolution of 300 μm per measuring station is assumed. A better estimate of the alignment error in a large iron spectrometer will be available after DØ has attempted to align its muon system. As a 300 μm resolution is readily attainable using modules with three planes of either drift chambers or 1 mm spaced MWPCs or PSFs, alignment errors are assumed to dominate the muon trajectory measurement.

Given an assumed resolution of 300 μm per measuring station, the momentum resolution due to position uncertainty can be calculated. In the central region, if a measurement using only the three muon stations is used, then a resolution of $0.32P_t$ is obtained. If the z-vertex is measured with a resolution of 1 mm, this gives a redundant measurement of the momentum with about the same dp/p. For the forward region,

the proposed chamber layout gives dp/p = 0.025p. This yields resolutions of $0.05P_t$ and $0.30P_t$ at $|\eta| = 1.5$ and $|\eta| = 3$ respectively. Figure III.D.2 shows the resolution for a 100 GeV P_t muon versus rapidity.

One final contribution to the resolution is radiative energy loss. It is shown in Appendix III.D.2 that an additional a 1.5% contribution is expected for energies less than 500 GeV.

III.D.3 Chamber Rates

Rates for muon detectors at the SSC have been thoroughly studied and reported in reference[III.D.2]. The report studied three sources of hits in muon detectors:

1. $\pi^{\pm}$, $K^{\pm}$, and K_L decays
2. prompt muons from c, b, t, and W decays
3. muons from hadronic showers (punch-through).

The above decay rates have been scaled from reference [III.D.2] to the ELMUD decay volume(see Appendix III.D.1).

The expected muon rates from all sources have been computed at chambers before the magnets(A-layer), after the magnets(B-layer), and at the last measuring station (C-layer). For ELMUD, the minimum iron thickness is about 23 λ. This thickness plus measuring the momentum after at least 5 λ of absorber and calorimeter reduces the rate from punchthroughs to an insignificant amount for all P_t.

The other source of hits in a muon detector is from indirect hadronic interactions, especially from small-angle items like the edges of the calorimeter, the beam pipe, and the low-β quads. These can give ten or more particles in the region $|\eta| = 2 - 3$. For ELMUD, from the muon detector point of view, the lack of a calorimeter in the forward region is a distinct advantage allowing the shielding in this region to be optimized. Also, the low-β quadrupoles are substantially upstream of the detector and should also be straightforward to shield.

While unwanted sources of muons can be eliminated offline, chamber cell sizes must be chosen so that pattern recognition is not impaired and so that the trigger threshold is above P_t of 10 GeV/c. The first question depends upon a detailed simulation of the muon system with pileup as well as use of a complete reconstruction program. Neither of these has been done so the cell sizes are based on hit rates in the chambers and on trigger rates. The rates found in Appendix III.D.1 have been used to compute chamber rates (assuming chambers subtend one quadrant in ϕ) for all three measurement stations in ELMUD. The results of this calculation are shown in Figure III.D.3 for a luminosity of $10^{34} cm^2\ s^{-1}$.

If a standard D$\emptyset$ muon chamber, which is 10 cm wide, is used as a reference then a hit rate of 1 kHz combined with a 1000 ns drift time gives a cell occupancy 0.1%. This occupancy is probably better than is needed. Nevertheless maintaining this clean occupancy was used a constraint. From Fig. III.D.3, one can conclude the following cell sizes are more than adequate: for $0 \leq |\eta| \leq 1.5$, 5 cm cells in A-layer and 10 cm cells in B/C-layers, for $1.5 \leq |\eta| \leq 2.5$, 1 cm cells in A-layer and 5 cm cells in B/C-layers, for $2.5 \leq |\eta| \leq 3$, 0.5 cm cells in A-layer and 0.5 cm cells in B/C-layers. It is clear that ELMUD, with quite conventional muon detector elements, can be expected to be robust up to the highest luminosities expected at the SSC.

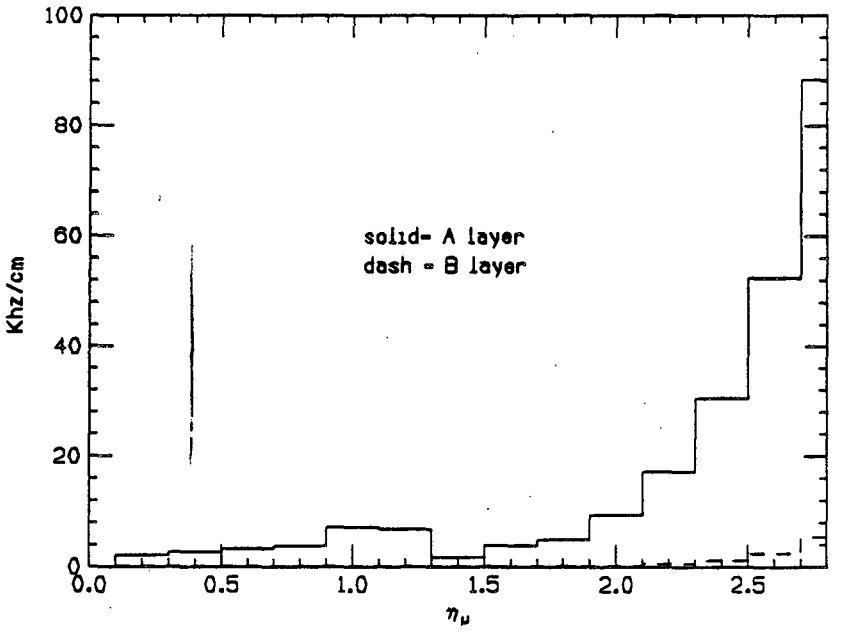

Figure III.D.3. Muon Rate at Chambers [KHz/cm] versus pseudorapidity [$|\eta_\mu|$] for: a) A-layer (solid), b) B-layer (dotdash) at 10^{34} cm^{-2} s^{-1} luminosity. By comparison, a tracker in front of calorimeter must contend with 3.5 MHz/cm at $10^{33} cm^{-2} s^{-1}$.

III.D.4 Costs

The cost of the muon system's magnets and chambers can be estimated either from the SSC guidelines[III.D.3] or the most recent cost summary of the DØ muon system. The values agree within 10%. The costs include installation and supporting equipment such as power supplies. Table III.D.2 gives the cost breakdown for the ELMUD muon system. The cost of the central toroid is about \$16M while that of both forward toroids is about \$3M. Some uncertainty exists in estimating the chamber costs. Drift chambers with cell sizes as given have been assumed. For the outer central region, this is clearly appropriate and we have assumed chambers similar to DØ with 3D readout. In the inner regions and at small angles, finely segmented devices (such as MWPCs or scintillating fibers) may be more amenable to the high rates. These will give a larger number of channels but with simpler electronics for each channel.

For comparison, the cost of super-ferric magnets in the forward region can be estimated by extrapolating from design work on air-core toroids[III.D.4]. The ELMUD coils are much smaller coils with different design goals and any estimates based upon this are very uncertain. Our estimate gives a cost for forward super-ferric magnets of about \$9M compared to \$3M for normal iron toroids. As there are clear advantages to super-ferric magnets in channels such as $H \rightarrow ZZ^*$, it would be preferable to use them if the cost differences were similar to the values given here.

Table III.D.2: Cost Table

item	unit cost	total
Cu absorber	\$3.5/lb	\$2.0M
central toroid, 9600 mt	\$1.4K/mt	\$13.5M
forward toroids, 1800 mt	\$1.4K/mt	\$2.5M
3000 m^2 of chambers	@\$2000/m^2	\$6.0M
18000 wires(4 readout/wire)	@\$80/channel	\$5.8M
20000 wires (single readout)	@\$100/channel	\$2.0M
fast trigger elements	@\$1.0M	\$1.0M
total		\$32.8M

III.E Trigger and Data Acquisition

III.E.1 Overall Architecture

The ELMUD trigger and data acquisition system is constrained by the bandwidths of the system at each point in the data path. Common to all detectors is the limitation bandwidth = event rate × event size. Bus structures are finite in their capacity, and do not appear to be increasing as rapidly in capacity as other technologies such as VLSI and CPUs. This sets a limit to the event size if a particular rate of data needs to be shipped or limits a detector to a smaller rate if the event size is large. In ELMUD, the event size is about 1/50 of that expected from a large general purpose detector. In this section a particular hierarchy of triggers is discussed. The details of what is done where are subject to the way hardware evolves over the next few years. Moreover, as confidence in the hardware is gained under real running conditions, downward migration of trigger software should be expected.

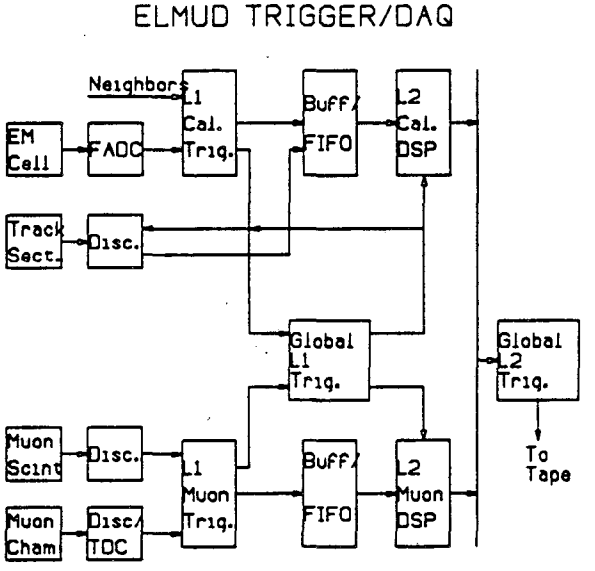

FIG. III.E.1 Trigger and data acquisition architecture for ELMUD.

At the front end of the detector the calorimeter and muon systems will have simple hardware to make a trigger decision in real time. The optimum strategy at this stage is to make a large number of local trigger decisions in parallel such as cluster and track finding. Upon receipt of this decision, digitization would commence followed by pipeline insertion. Whenever possible, the flash digitized data used by the trigger should be the same as that used in final analysis thereby making the study of trigger efficiency straightforward. Prior to writing the event to tape there is a need to bring the entire event together and make a trigger decision. The level-2 trigger processor would in this case collect all the trigger information for an event in the form a bit pattern. This pattern would then be compared to a list of desired patterns and,

if necessary, call for the event data to be assembled and transferred to a mass storage medium for offline analysis.

III.E.2 Electron Photon Trigger

In ELMUD, an important physics goal at a luminosity of $10^{33} cm^{-2} s^{-1}$ is the channel $H \rightarrow \gamma\gamma$. The level-1 calorimeter trigger signal will consist of analog sums of cells designed to find clusters of electromagnetic energy isolated from other energy within a radius of 0.2. For a staggered pattern of calorimeter cells, each cell forms a sum with three neighbors to make a quad as shown in (Fig III.E.2). Each cell participates in four quads so that the trigger is fully efficient for particles hitting between cells. A quad is compared to its six nearest neighbors to determine the local maximum. In parallel, the sum of the six nearest non-overlapping quads is formed. The ratio of this sum to the central quad is a measure of the isolation. The quad energy and isolation ratio are discriminated and form a coincidence which constitutes the level-1 electron/photon trigger. For electrons and photons, the dominant source of triggers is expected to be from QCD jets themselves. Isolated in this case means that the ratio of energy in the neighboring trigger cells of the central quad over the sum of that in the central quad plus its nearest neighbors is less than 0.10. For single clusters with E_t >20 GeV and crude isolation, the level-1 trigger allows a rate of 20 KHz.

At level-2, additional crude shower shape cuts based on energy deposits in each of the calorimeter cells composing the quad yield a rate of roughly 10 Khz for single clusters and over 200 Hz for two clusters. Any post EM calorimeter radiator cuts, crude di-cluster mass cuts, or opening angle criteria will most likely reduce triggers to acceptable rates (100 Hz). Other single EM cluster triggers with larger E_t cuts are possible. Figure III.E.3 shows the integrated rates versus E_t thresholds for the most energetic isolated EM trigger cell and the two most energetic isolated EM trigger cells after level-1 and -2 triggers.

III.E.3. Muon Trigger

The level-1 muon trigger will begin with a scintillator element identifying a muon outside of the iron toroids. In the central region these elements can be large since the rate is low. The scintillator size can be scaled to match the rate from muons in that region. In the forward region, two layers of scintillator will be used to reduce the rate from scraping particles. The scintillator system will provide a gate and common stop for the drift tubes. Latched hodoscopic information from each tube in a modest road can be combined with the scintillator information in that road to make a crude momentum determination of the muon. A good track can initiate conversion of the drift times in a TDC and the occurrence of a track can be sent to the global level-2 trigger.

The level-2 muon trigger will utilize the fully digitized information of the event. It should be possible to achieve a stringent muon momentum cut at this level and also to correlate tracks in di-muon events. Figure III.E.4 shows the integrated trigger rate as a function of P_t threshold for the highest P_t muon and for the two highest P_t muons. A P_t threshold of 20 GeV cuts the level-2 rate to a few Hz at a luminosity of $10^{33} cm^{-2} sec^{-1}$.

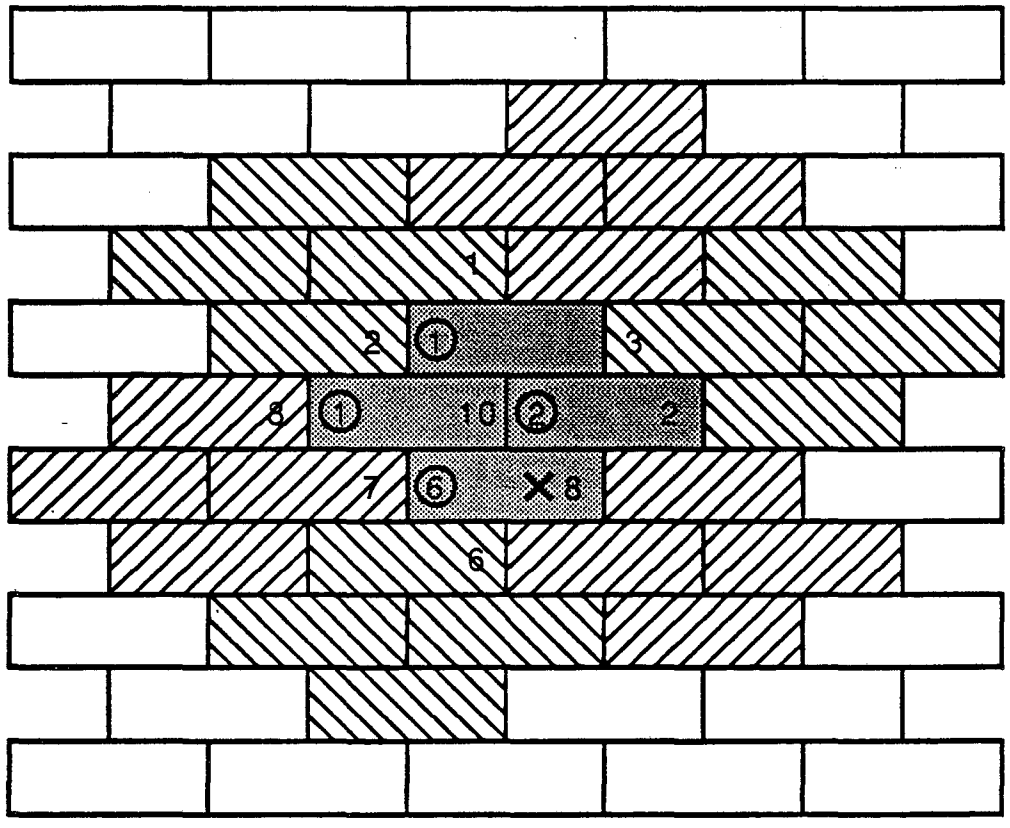

FIG. III.E.2 Calorimeter trigger. The X represents the impact point of a 10 GeV electromagnetic shower. Energies of 1,1,2, and 6 GeV are deposited in the shaded calorimeter cells. The numbers in the cells are quad sums and the hashed areas are the cells summed for isolation.

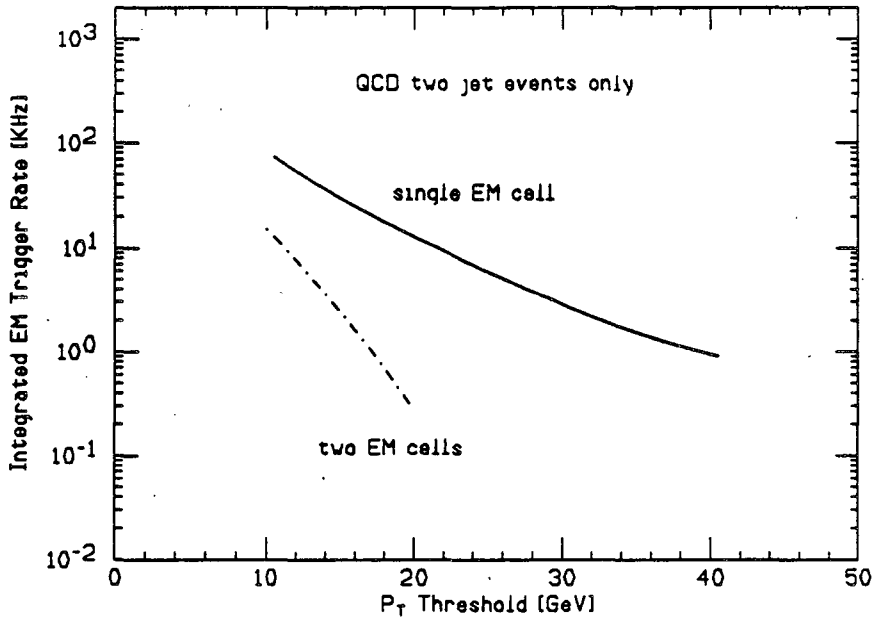

FIG. III.E.3 Integrated highest P_t EM cell Rate vs. P_t thresholds in ELMUD *at $10^{33} cm^{-2} s^{-1}$ luminosity. Both single highest E_t EM cell and two highest E_t EM cell rates are shown.*

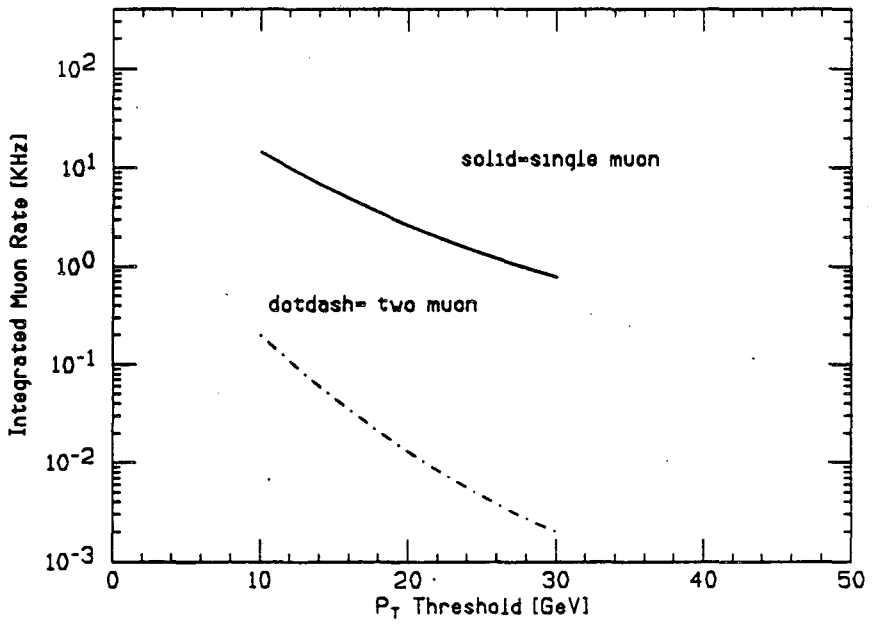

Figure III.E.4 Integrated Muon Trigger Rate vs P_t threshold at $10^{33} cm^{-2} s^{-1}$ luminosity. Both single and di-muon rates shown. Sources shown are from prompt c and b decays.

References

I.0 F. Paige, From Colliders to Supercolliders, Madison,(1987).

I.1 R. Thun et al., Experiments, Detectors, and Experimental Areas for the Supercollider, Berkeley, July (1987),R. Donaldson and G. Gilchriese Eds.

I.2 G. Kane, talk given at Tuscon, 1990.

II.1 D. Atwood et al., in Ref I.1.

II.2 C. Barter et al., Proceedings of the Summer Study on High Energy Physics in the 1990s,Snowmass, June(1988), S.Jensen, Ed.

II.3 J. Gunion et al., Nuc.Phys. B299,(1988).

II.4 Expression of Interest to the Superconducting Super Collider Laboratory by the L* Collaboration May (1990).

II.5 J. Gunion et al., Higgs Hunter Guide,(1989).

II.6 E. Wang et al., Proceedings of the Summer Study on High Energy Physics in the 1990s,Snowmass, June(1988), S.Jensen, Ed.

II.7 R. Cahn et al., Experiments, Detectors, and Experimental Areas for the Supercollider, Berkeley, July (1987),R. Donaldson and G. Gilchriese Eds.

II.8 J. Bensinger et al., May (1990), SSC-SDC-39 or SSC-287.

II.9 H-U.Bengtsson and T.Sjostrand, Proceedings of the Summer Study on High Energy Physics in the 1990s,Snowmass, June(1988), S.Jensen, Ed.

II.10 F. Paige and S. Protopopescu,Proceedings of the Summer Study on High Energy Physics in the 1990s,Snowmass, June(1988), S.Jensen, Ed.

II.11 PAPAGENO is written by Ian Hinchliffe. Documentation is on computer disk file.

II.12 G. Altarelli et al., Z.Physik C45 (1989) 109.

II.13 E. Eichten et al., Rev. Mod. Phys. 56 (1984) 579.

II.14 F. Abe et al., Phys.Rev.Lett. 63 (1990) 147.

II.15 R. Chivukula, Proceedings of the Summer Study on High Energy Physics in the 1990s,Snowmass, June(1988), S.Jensen, Ed.

II.16 J. Owens, private comm. (1990).

II.17 J. Bagger et al., FNAL Conf-90/253.

III.B.1 A more detailed discussion in contained in the DØ Upgrade Proposal, Fermilab, 1990.

III.B.2 K. Johnson et al. IEEE Trans. Nucl. Sci. 37-2 (1990) 500

III.B.3 S. Reucroft, Proceedings of the Ft. Worth Symposium on Detector Development for the SSC, Ft. Worth, 1990.

III.B.4 M. Salomon, in Ref III.B.3.

III.B.5 EMPACT Letter-of-Intent, SSC LoI 3, Nov 1990.

III.C.1 R. Wigmans, NIM A269 (1987) 275

III.C.2 D. Hertzog et al., NIM A294 (1990) 466

III.C.3 D. Groom, Proceedings of the Workshop on Radiation Damage, Tallahassee, (1990), K. Johnson Ed.

III.C.4 A. Acosta et al., NIM A294 (1990) 193

III.C.5 D. Anderson FERMILAB 89/189 (1989)

III.C.6 C. Woody et al., IEEE Trans. Nucl. Sci. NS-36 (1989) 536

*III.C.*7 H. Yamamoto, Proceedings of the International Conference on Calorimetry in High Energy Physics, Fermilab, Nov 1989.
*III.C.*8 H. Piecarz, in Ref III.C.6
*III.C.*9 H.Gordon et al., SSC R&D Subsystem Proposal to Study Liquid Argon
*III.C.*10 R. Brun, Geant312 Users Guide
*III.C.*11 S. Linn, SSCSIM Users Guide SCRI 89/1
*III.C.*12 P. Mocket, Proceedings of the Summer Institute, SLAC (1983) 367
*III.D.*1 C. Brown et al., NIM A279 (1987) 331; DØ upgrade proposal, November 1990.
*III.D.*2 D. Green and D. Hedin, NIM A297 (1989) 111.
*III.D.*3 M. Gilchriese, Tuscon, 1990.
*III.D.*4 About half the cost of a superconducting coil is due to the amount of superconducting cable used with the other half due to the cost of the cryostat and the mechanical supports. A rough parameterization of the coil designs in the EMPACT EOI gives $Cost(M\$) = 0.2(L + R_o - R_i) \times (2B_iR_i + R_o + R_i)$ with L, R_o, and R_i being the toroid's length, outer radius, and inner radius (in meters) and B_i being the magnetic field at R_i (in Tesla).
*III.D.*5 J. Eastman and S. Loken, in Ref. II.1.
*III.D.*6 W. Lohmann, R. Kopp, R. Voss, CERN85-03.
*III.D.*7 S. Abachi, private communication.
*III.D.*8 D. Carlsmith et al., Snowmass 1986.

Appendices

Appendix II.A Isolation in ELMUD

ELMUD relies on the EM calorimeter being sufficient for background rejection. Over half (1/3 from π^0 plus 1/3 of 2/3 from $\pi^{\pm}$) of energy of a jet is deposited in an EM calorimeter on the average. The longitudinal distribution of energy(including fluctuations) was modeled to agree with a full simulation and test data to test this hypothesis. The effectiveness of isolation cuts at rejecting a typical background ($t\bar{t}$) using EM only versus full energy containment is shown in Figure AIIA.1. A given cut on the transverse energy in a cone shows only a factor of two difference over a full calorimeter. An important check is to see how well isolation rejection works when electron shower spreading is incorporated. Presumably this means wider cones (and additional loss in signal acceptance) but it is not known how serious this will be.

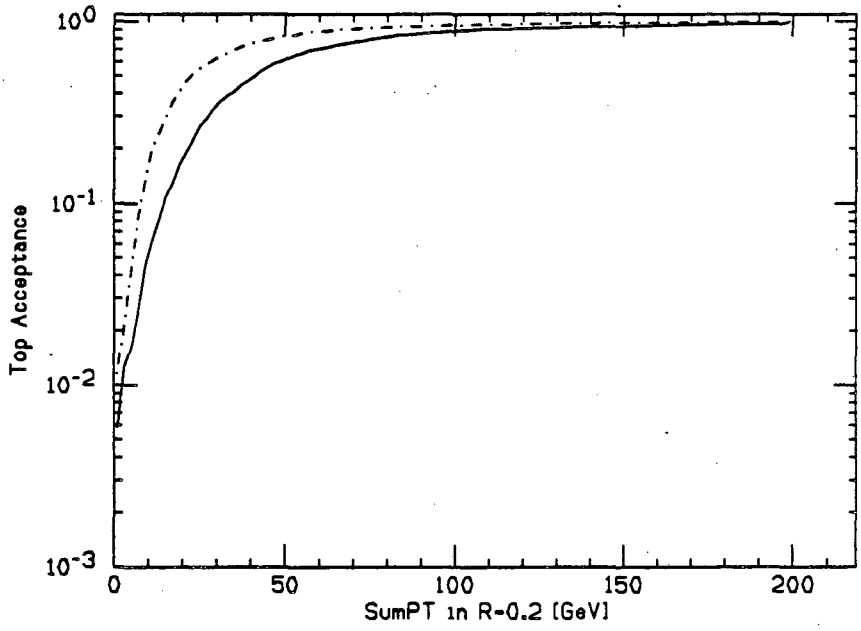

FIG. AII.A.1 Top Rejection using isolation cuts with full (solid) and EM only (dotdash) calorimeter. Charged hadron energy in calorimeter is treated with proper longitudinal fluctuations.

Appendix II.B New Gauge Bosons

A new Z-boson that decays via lepton pair will be seen as a peak in the di-lepton (e or μ) mass spectra. The model from ref. [II.12] is implemented in Pythia 5.4. Backgrounds to this are Drell-Yan pair production. Invariant mass plots for di-leptons

in ELMUD for a 1 TeV and 4 TeV Z' are shown in Figure AII.B.1. The electron mode shows a sharp peak and the muon mode shows a degraded peak (recall dP/P=0.11 + $0.3P_t$ [TeV]). If sufficient statistics are available, then asymmetry measurements using the muon mode will be possible.

Single high P_t lepton from new W-bosons will be seen in ELMUD. A plot of the Jacobian peak in $P_{t,\mu}$ of a 1 TeV W' is shown in Figure AII.B.2 below. The expected backgrounds $t\bar{t}$, $b\bar{b}$ and $c\bar{c}$ are also included. It is clear than that ELMUD will have good sensitivity to new W-bosons if they decay into electrons or muons.

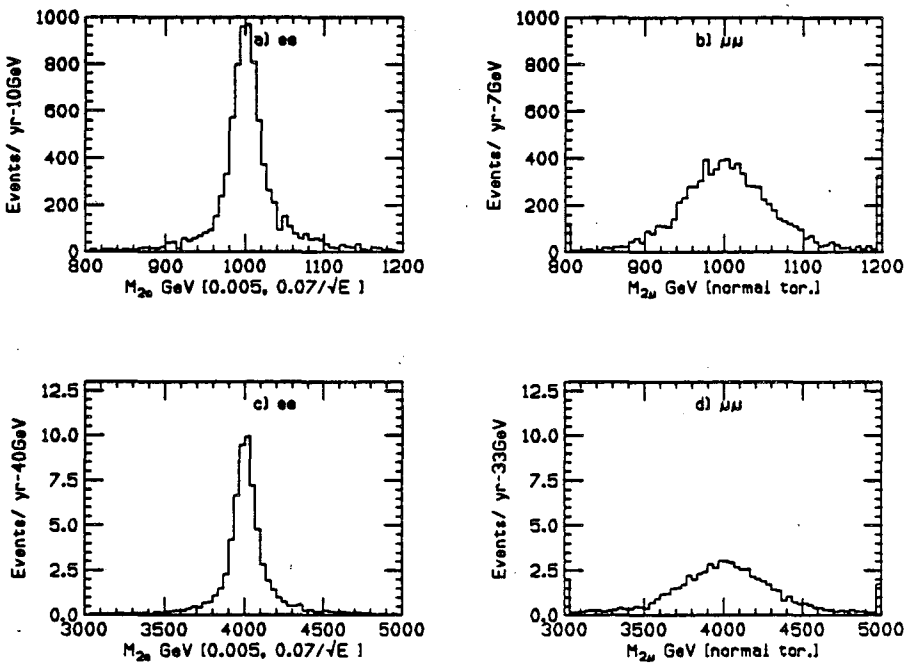

FIG. AII.B.1 Di-lepton mass spectra for Z' for (a) ee mode, $M_{Z'} = 1\ TeV$, (b) $\mu\mu$ mode, $M_{Z'} = 1\ TeV$, (c) ee mode, $M_{Z'} = 4\ TeV$ and (d) $\mu\mu$ mode, $M_{Z'} = 4\ TeV$.

Appendix II.C Compositeness

With ELMUD, one will be able to perform compositeness searches for a restricted class(leptons) of physics processes. Following the discussion in ref. [II.13], a flattening of the di-lepton mass distribution at very high ($>$ 1 TeV) mass regions signals the onset of a new scale. Without compositeness the di-lepton spectra will be pure Drell-Yan:

$$q\bar{q} \rightarrow \gamma/Z \rightarrow l\bar{l}$$

Figure AII.C.1 shows the M_{2lep} spectra for e or μ modes adapted from ref. [II.13] for one SSC year running. Using the criteria in ref.II.13 for ascribing excess events as compared to that expected with no compositeness, the compositeness scale limit is $\sim$ 25 TeV. This search mode is clean and not subject to calorimeter non-linearities.

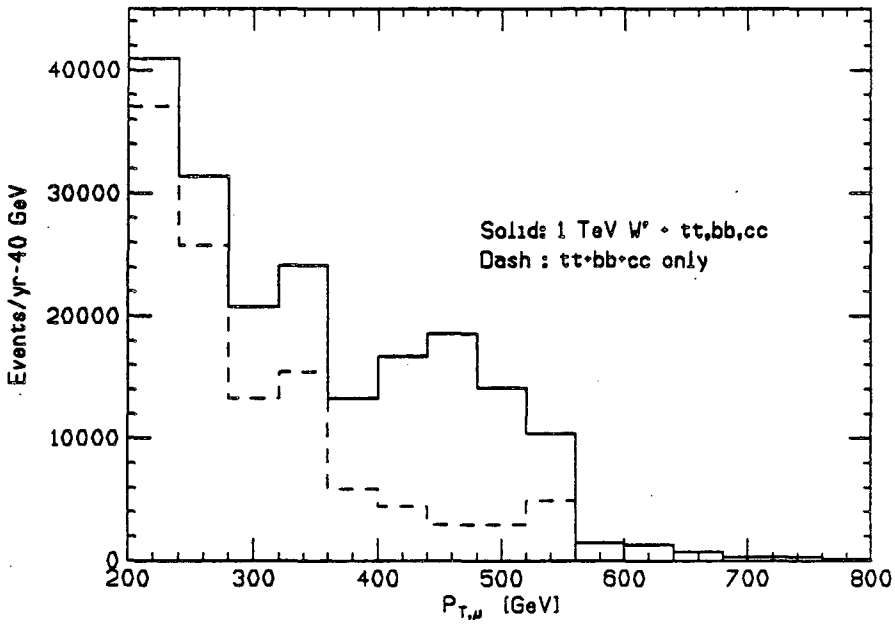

FIG. AII.B.2 Muon P_t spectra for 1 TeV W' . Also included are $t\bar{t}, b\bar{b}$ and $c\bar{c}$ backgrounds.

It may be possible to study quark compositeness by an accurate measurement of the P_t spectrum of direct photon and π^0 production. In general, these cross-sections are predicted by QCD perturbative calculations, and deviations from the QCD cross-section would be signals of a new scale. Photon and π^0-jet physics will be a useful physics benchmark for the detector to study fragmentation functions and other fundamental QCD calculations extended to the highest energy. Lastly, the study of single isolated photons is a well-predicted QCD process with lower uncertainty than the calculations of jet physics. Since ELMUD will have a highly efficient trigger for relatively low-P_t photons, measurements of the low-x portion of the gluon structure function will also be possible.

Appendix II.D Top

It is ironic that many SSC studies treats the top quark as an unwanted background to *interesting* physics and yet remains undiscovered. If it is a background, then it can be seen. The top decay channel most readily observed is [II.14]:

$$t\bar{t} \rightarrow W^+W^- + b\bar{b} \rightarrow e + \mu + X$$

The largest backgrounds expected are:

$$\begin{aligned} q\bar{q} &\rightarrow \tau + \bar{\tau} \rightarrow e + \mu \\ q\bar{q} &\rightarrow W^+W^- \rightarrow e + \mu \end{aligned}$$

The analysis basically consists of searching for an isolated e and μ that both have substantial P_t. Backgrounds either have small P_t leptons and may be non-isolated.

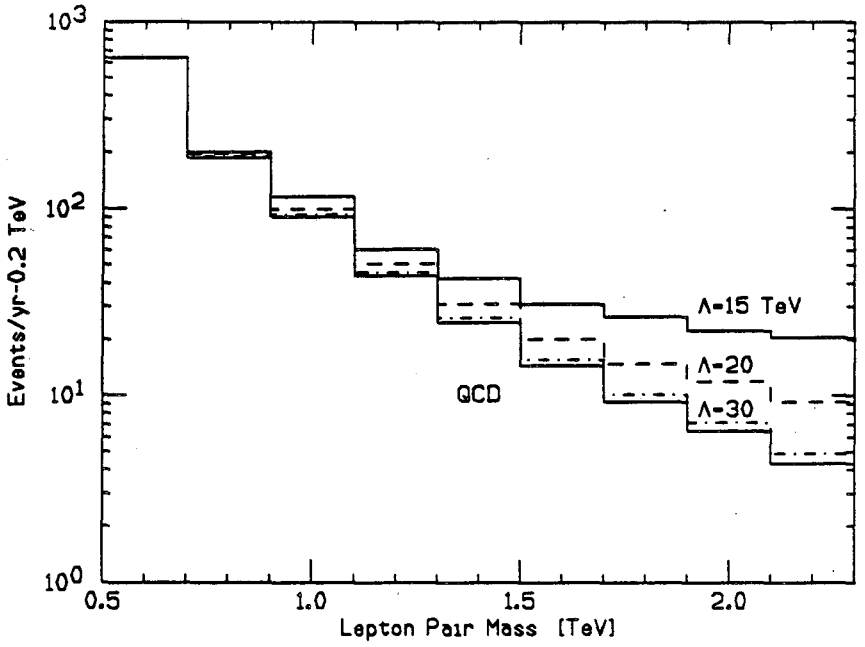

FIG. AII.C.1 Di-lepton mass spectra for different Compositeness scales, Λ adapted from ref. [II.13].

In a $P_{t,e}$ vs. $P_{t,\mu}$ plot, the signal populates the region of large P_t. Figure AII.D.1a shows the integrated cross section versus lepton P_t cut.

A study was also undertaken of $t\bar{t} \rightarrow 2\mu +$ X. Here potential backgrounds arise from Drell-Yan, $b\bar{b}$ and $c\bar{c}$. Isolation cuts remove the heavy quark backgrounds and a cut on the absolute value of the vector P_t sum of the muons removes Drell-Yan because it peaks at zero, whereas the signal is broad(See Figure AII.D.1b.) If an isolation cut of 5 GeV in a cone of R=0.2 is used, then a clear signal for a 140 GeV top is seen in the minimum $P_{t,\mu}$ distribution. For a 250 GeV top however, Drell-Yan backgrounds become comparable to signal and more careful background studies will be required. See Figure AII.D.1c. The conclusion is that top will manifest itself even in the 2μ (or 2e though not studied) mode and will be observable in ELMUD.

Appendix II.E Technicolor

A relatively naive view of technicolor considers one doublet of technifermions, $\binom{U}{D}$ which in an analogous way to QCD, can combine and form:

ρ_T	$\rightarrow$	W^+W^-	ref. [II.13]
$\rho_T^{\pm}$	$\rightarrow$	$W^{\pm} + Z$	ref. [II.13]
ω_T	$\rightarrow$	$Z + \gamma$	ref. [II.15]

The masses are generally $O(1\ TeV)$. The ρ_T appears with low rate ($\sim$ 10 events per year into lepton mode) as a broad resonance ($\sim$ 300 GeV). Recent studies [II.17]

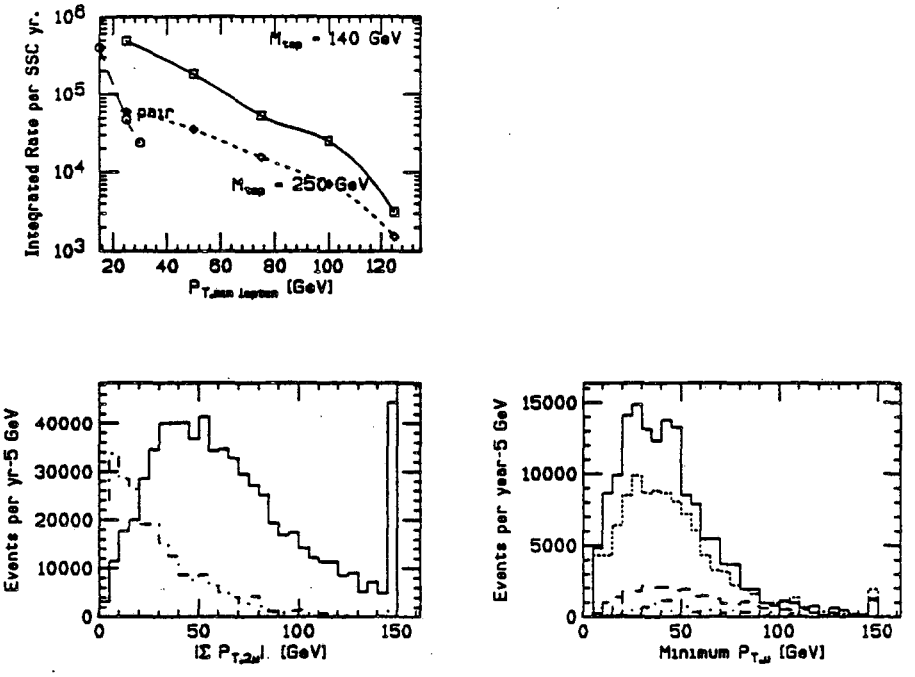

FIG. AII.D.1 (a)Integrated top cross section in the $e + \mu$ mode for given lepton P_t cut for $M_{top} = 140$ and 250 GeV. Tau pair background is also shown. (b) $|\Sigma\vec{P}_{t,\mu}|$ distribution for $t\bar{t}[M = 140\ GeV]$(solid) and Drell-Yan(dotdash). (c) P_t of slowest μ for $t\bar{t}$, Drell-Yan and $b\bar{b}, c\bar{c}$(dotdash) for 140(solid), 160(dots) and 250(dashes) GeV top masses. Leptons are required to be inside ELMUD *geometry and must be isolated.*

indicate that a clean signal can be expected for ρ_T, but this has not been studied by us. The ω_T ,on the other hand, decays into a very narrow ($< 4\ GeV$) reconstructable state (i.e. 2 electrons + one photon) in ELMUD. The expected $Z + \gamma$ background is smaller than signal when $M_{\omega_T} < 2.6\ TeV$. The mass plot of $M_{\gamma+Z}$ appears in Figure AII.E.1a-b.

Appendix II.F Monte Carlos

A number of generators have been used in this study and a summary of the particular processes used are documented below so that further details of the physics assumptions can be pursued by the reader if desired.

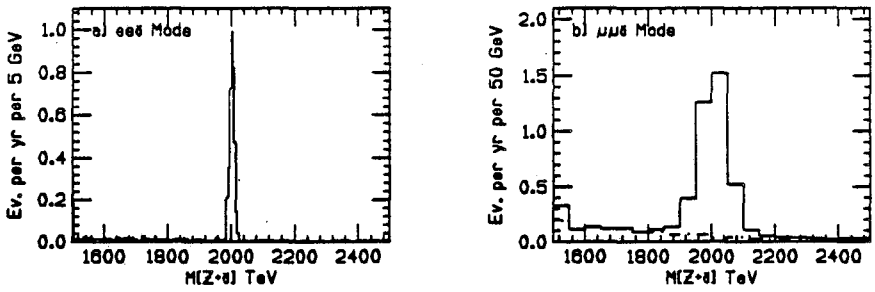

FIG. AII.E.1 Invariant mass $M_{Z\gamma}$ for technirho inside ELMUD *in (a) $ee+\gamma$ mode and (b) $\mu\mu+\gamma$ mode.*

Monte Carlos*

Process:	PYTHIA ref. [II.9]	ISAJET ref. [II.10]	PAPAGENO ref. [II.11]	OWENS ref. [II.16]
$H \to 2\gamma$	√			
$q\bar{q} \to 2\gamma$	√		√	√
$gg \to 2\gamma$	√		√	√
$g+$ jet	√			
$gg \to q\bar{q}+\gamma$				√
$gg \to$ [hard]π^0 + X				√
$gg \to$ [hard]$2\pi^0$ + X				√
jet + jet	√	√		
$H \to ZZ^*$	√			
$H \to ZZ$	√	√	√	
$q\bar{q} \to ZZ$	√	√	√	
$Z + t\bar{t}$			√	
$Z + b\bar{b}$			√	
$Z+$ jet	√	√		
$gg \to t\bar{t}$	√	√	√	
$gg \to b\bar{b}$	√	√	√	
$gg \to c\bar{c}$	√	√	√	
$q\bar{q} \to Z$	√	√	√	
$q\bar{q} \to Z'$	√			
$q\bar{q} \to W'$	√			

* A check (√) means either used explicitly or checked with each other.

Appendix III.D.1 Muon Cross Sections in ELMUD

Muon rates versus absorber thickness assuming a cylindrical decay volume with a radius of 50 cm and length of 100 cm are shown in Table III.D.5. Rates are in

μb summed over all P_t and λ_0 is in proton units. Table III.D.5 is adapted from Ref[III.D.2] by scaling the decay rates for the ELMUD geometry.

Table III.D.5: Muon Cross Sections in μb

Thickness(λ_0)	Source	$0 \leq \|\eta\| \leq 1$	$1 \leq \|\eta\| \leq 2$	$2 \leq \|\eta\| \leq 3$
9	decay	60	710	3700
	punch	70	420	4400
	prompt	20	130	300
	all	150	1300	8400
12	decay	50	510	2900
	punch	5	30	400
	prompt	15	130	300
	all	70	670	3600
21	decay	8	80	740
	punch	-	-	1
	prompt	10	70	200
	all	18	150	940
25	decay	4	40	440
	punch	-	-	-
	prompt	10	70	190
	all	14	110	630
35	decay	1	12	135
	punch	-	-	-
	prompt	7	10	135
	all	8	22	270

Appendix III.D.2 Radiative Energy Loss

A number of authors[III.D.5,6] have studied muon energy loss in material at large muon energies. Above some critical energy (about 300 GeV in iron and 80 GeV in uranium), the contributions from radiative processes such as bremstrahlung dominate over ionization. These authors show that the average energy loss above the critical energy is essentially proportional to the muon energy.

Studies of the variation in energy loss are not known to us so Geant was used to simulate the passage of muons (energies of 200, 500, 1000, 2000, 4000 GeV) through 11.3 λ of iron (1.95 m) and uranium (1.37 m). For each of the materials, the energy loss distributions scaled by the muon energy (that is E_{lost}/E_μ) were very similar for different energies. Table III.D.3 characterizes the energy loss distributions in terms of the half-width at half maximum (hwhm) and root mean square (rms). It also gives the fraction of events which had greater than 10% energy loss. Within the statistics (1000 events for each energy), the values are energy independent. It was found that the average energy loss as predicted by Geant were systematically lower, at the very high energies, than Ref[III.D.6]. Following this study, it was determined that be lowering the cutoff parameters in GEANT, agreement with Ref[III.D.6] could be obtained[III.D.7].

TABLE III.D.3: Muon Energy Loss

p(GeV)	200	500	1000	2000	4000
1.95 m Fe					
$E_{loss}(GeV)$	4.8	7.9	11.4	20.8	39.0
$rms/E_\mu(\%)$	1.7	1.5	1.0	1.0	1.0
$hwhm/E_\mu(\%)$	0.5	0.6	0.4	0.5	0.4
$E_{loss}/E_\mu \geq 10\%$	1.4	1.6	0.9	1.6	1.2
1.37 m U					
$E_{loss}(GeV)$	12.3	23.3	42.0	78.	146
$rms/E_\mu(\%)$	2.8	2.8	2.6%	2.5	2.3
$hwhm/E_\mu(\%)$	2.2	1.8	1.8%	1.8	1.7
$E_{loss}/E_\mu \geq 10\%$	8.2	7.9	8.3%	7.4	7.9

There are a number of interesting results. The first is that the energy loss divided by the muon energy is energy independent. As dp/p is usually the parameter of interest, this says that the effect of energy loss on muon energy resolution is independent of energy once one is above the critical energy (which is essentially everything of interest at the SSC). This is different than the usual statement which says that muon energy loss becomes more important at higher muon energies.

If the energy loss in the absorber is un-measured, then the variation in energy loss will set a lower limit on the muon resolution (about 2.5% for uranium) in the absence of calorimetric energy measurements. This effect must be added in quadrature to the other resolution effects taking into account the non-Gaussian nature. For ELMUD, the fluctuations in energy loss will add about 1.5% to the energy resolution . There will also be losses of about 4% due to events with large energy losses. One of the additional advantages of using a super-ferric magnet in the forward region is its reduction in the amount of iron from 6 m to 2 m. This will decrease the inefficiency due to muons with large energy losses.

The other effect of energy loss is the presence of electromagnetic showers accompanying the muon. Here the amount of energy is proportional to the muon energy and so this presents greater problems at higher muon energies. These showers can wipe out muon measurements and so force additional measurement layers for redundancy. Previous studies of this[III.D.5,8] usually assumed the worst case; that an accompanying shower always causes the muon information to be lost. This led to an inefficiency of about 5% in each layer for a 1 TeV muon. The current ELMUD design uses the vertex point, the inner tracking measurement, and three muon measurement stations to give a trajectory. If any one of the muon stations is lost, the muon momentum can still be determined though with an energy-dependent worsening of the resolution. In the forward region, the muon momentum is larger, and so additional measurement planes are placed before the magnet and between the two toroids. Studies of the triggering and offline reconstruction efficiencies versus muon momentum need to be performed to determine if this level of redundancy is sufficient.